Supplementary Information (SI) for Energy & Environmental Science.
This journal is © The Royal Society of Chemistry 2025

Supporting Information

Single Ion Conductive "Plasticine-Like" Solid Electrolyte Combined with Modulated D-Band Center of Interfacial Zinc Atoms for Highly Reversible Zinc Metal Anode

Kang Yan[1,2], Yongbo Fan[3], Xueya Yang[2], Xinyu Wang[1], Shengmei Chen[4], Weijia Wang[2], Mingchang Zhang[5], Huiqing Fan[2]*, Longtao Ma[1]**

[1] School of Materials Science and Engineering, Guangdong Provincial Key Laboratory of Advanced Energy Storage Materials, South China University of Technology, Guangzhou 510641, P. R. China.

[2] State Key Laboratory of Solidification Processing, School of Materials Science and Engineering, Northwestern Polytechnical University, Xi'an 710072, P. R. China

[3]Department of Applied Physics, The Hong Kong Polytechnic University, Hung Hom, Hong Kong, P.R. China.

[4]Department of Materials Science and Engineering, City University of Hong Kong, Kowloon, Hong Kong, P. R. China.

[5] Institute of Science and Technology for New Energy, Xi' an Technological University, Xi' an 710021, P. R. China

Corresponding authors: fanybmail@163.com, hqfan@nwpu.edu.cn, longtaoma@scut.edu.cn

Experimental section

1. Preparation of the “plasticine-like” solid electrolyte（PLSE）

To prepare the “plasticine-like” solid electrolyte (PLSE), commercial polyacrylonitrile (PAN, Sinopharm Chemical Reagent Co., Ltd.), anhydrous $ZnCl_2$ (Sinopharm Chemical Reagent Co., Ltd.), and $InCl_3·4H_2O$ (Sinopharm Chemical Reagent Co., Ltd.) were mixed in specific proportions. The required amount of deionized water was measured using a pipette. Deionized water was then added to the mixture, which was stirred continuously at 60°C until fully dissolved. To further improve miscibility, a mortar and pestle were used during the process.

The resulting "plasticine-like" solid electrolyte was labeled as PLSE-In, PLSE, and 30 m $ZnCl_2$, respectively, and stored in a vacuum-dried jar for future use. The main preparation steps, along with optical images and mechanical properties of PLSE, are shown in **Figs. S1, S2, and S3**.

In this study, PLSE with varying PAN and indium contents were prepared separately to determine the optimal ratios. These variants were designated as PLSE-In1 and PLSE-In2. The optimal PLSE-In was selected based on the cycling performance of Zn||Zn symmetric cells. The material ratios and key preparation steps are detailed in **Tab.S1**.

Tab. S1 Summary table of simplified names and corresponding material ratio of prepared the plasticine-like solid electrolyte (PLSE)

Detailed Name		$ZnCl_2$ (g)	H_2O (g)	PAN (g)	$InCl_3·4H_2O$ (g)	In:Zn (mole)
relative molecular mass		136.3	18.0	426.0	293.2	/
Research contents	PLSE-In (43 m $ZnCl_2$)	5.84	0.98	0.20	0.10	0.01:0.99

	PLSE (43 m $ZnCl_2$)	5.84	1.00	0.20	0.00	/
	30 m $ZnCl_2$	4.09	1.00	0.00	0.00	/
Determine ratio	PLSE-In1 (43 m $ZnCl_2$)	5.84	0.95	0.20	0.20	0.02:0.98
	PLSE-In2 (43 m $ZnCl_2$)	5.84	0.98	0.40	0.10	0.01:0.99

m=Molar quantity $_{ZnCl2}$/Mass $_{H2O}$

2. Preparation of I_2@AC

Coconut shell carbon and iodine monomers (Sinopharm Chemical Reagent Co., Ltd.) were ground and mixed at a mass ratio of 1:4. The mixture was then transferred to a reaction kettle and heated at 100°C for 10 hours in a pit-type furnace. Afterward, it was allowed to cool to room temperature, yielding I_2@AC. The iodine loading ratio was determined through thermogravimetric analysis **(Fig. S4)**[1].

3. Cell assembles

All electrochemical performance tests in this experiment were conducted using a two-electrode system. Due to the corrosive nature of chloride, the tests were carried out with pouch-type batteries. The assembly process for these flexible pouch-type batteries is shown in **Fig. S5**. Zn||Br_2 cells were prepared using the same method, with tetrabutylammonium tribromide (Sinopharm Chemical Reagent Co., Ltd.) as the active substance.

3.1 The fabrication of half batteries

All electrochemical performance tests in this experiment were conducted using a two-electrode system. Except for the Zn||Zn symmetric and full batteries, other half-cells were assembled using inert electrodes. The specific assembly process for each test is as follows: Ti||Ti for ionic conductivity, Zn||Zn for ion mobility, Zn||Cu for Coulombic efficiency, Zn||Zn for the I-t curve, Zn||Ti for the LSV curve, Zn||Zn for the Tafel curve, and Zn||Cu for the CV curve of the half-cell.

3.2 The construction of full batteries

The materials were weighed in a ratio of I_2@AC: conductive carbon black: PVDF = 8:1:1 (wt), then placed in an agate mortar and ground repeatedly with an appropriate amount of NMP until the mixture became uniform and viscoelastic. The resulting slurry was coated onto a 1 cm^2 area of carbon fiber cloth and cut into 2 cm^2 square pieces with polar lugs. The electrodes were then dried at room temperature for 12 hours before use. The battery was assembled using these electrode plates as the cathode and 10 μm-thick zinc metal foil (5.85 $mAh \cdot cm^{-2}$) as the anode. The loading mass of active materials is set at 4 $mg \cdot cm^{-2}$ (1.8 $mAh \cdot cm^{-2}$), reaching a practical N/P ratio of 3.25. Zn||Br_2 cells were prepared using the same method, with tetrabutylammonium tribromide (Sinopharm Chemical Reagent Co., Ltd.) as the active substance. The loading mass of active materials is set at 7.5 $mg \cdot cm^{-2}$ (1.8 $mAh \cdot cm^{-2}$), maintaining a practical N/P ratio of 3.25 with Zn||I_2 cells.

4. Characterization of anti-catalytic properties

A three-electrode configuration was employed to test hydrogen evolution. LSV and Tafel curves were used to characterize the anti-catalytic properties of the In-rich solid electrolyte interphase (In-rich SEI). Zn||Zn symmetric cells were cycled for 50 hours at 0.5 mA·cm^{-2} and 0.25 mAh·cm^{-2} using PLSE-In, PLSE, and 30 m $ZnCl_2$ aqueous electrolyte. After cycling, the electrodes were cut to a 1 cm^2 area and used as the working electrode, with a Pt plate as the counter electrode, an Ag/AgCl electrode as the reference, and a 7 m NaCl aqueous solution as the electrolyte to minimize Zn^{2+} interference and maintain a highly concentrated salt environment. To focus on the role of the In-rich SEI, Zn electrodes cycled with PLSE-In and PLSE were labeled as Zn-In and Zn, respectively.

5. Electrochemical measurements

Ion conductivity, ion transfer number, LSV curves, Tafel curves (including those for characterizing the anti-catalytic properties of the In-rich SEI), electrochemical impedance spectroscopy (EIS, to study the evolution of the indium-rich SEI), I-t curves, and CV curves were measured using the Scott Electrochemical Workstation (CS2350M). The evolved hydrogen from zinc foils with different interfacial phases was detected using a gas chromatograph (Agilent 7890A). Cyclic stability, multiplier performance, Coulombic efficiency, and GCD curves were assessed with the Land battery measurement system (3002A, Wuhan, China).

5.1 Measurement method of ionic conductivity

The Ti||SPEs||Ti cell was used to test ionic conductivity with EIS frequency range 0.01 Hz ~ 100 KHz and amplitude of 10 mV. The computation formula is as follows:

$$\sigma = \frac{d}{RS} \tag{1}$$

Where *σ*, *d*, *R* and *S* represent ionic conductivity, the thickness of electrolytes (0.1 cm), A. C. resistance, and the area of PLSE (1 cm^2), respectively.

5.2 Measurement method of ion migration number

Ion transfer number was calculated using the Evans-Vincent-Bruce equation:

$$t_{Zn^{2+}} = \frac{I_S(\Delta V - I_0 R_0)}{I_0(\Delta V - I_S R_S)} \tag{2}$$

Where $t_{\mathrm{Zn}}{}^{2+}$ represents the ion transfer number, R_0 and I_0 are the A. C. resistance and initial current before potentiopolarization, while $\mathrm{R_s}$ and $\mathrm{I_s}$ are the reaction resistance and stable current after potentiopolarization, respectively. The potential difference is denoted as ΔV. For the EIS test, the frequency range was 350Hz~100 KHz with an amplitude of 10 mV and the potentiopolarization potential of 10 mV. The fitting circuit is as follows:

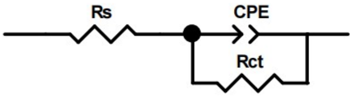

5.3 Activation energy of ionic conductivity

The activation energy of ionic conductivity can be fitted with Arrhenius equation:

$$\sigma = \sigma_0 \exp(\frac{-E_a}{kT}) \tag{3}$$

Where σ is ionic conductivity, σ_0 is exponential pre-factor, which is related to the number of carriers. The E_a is the activation energy of Zn^{2+} ionic conductivity, *k* and *T* are Boltzmann constant and temperature, respectively.

5.4 Analytical method of Tafel slope (b)

$$b=\frac{\partial_{\eta}}{\partial_{Logi}}=\frac{2.303RT}{\alpha F} \tag{4}$$

where b is the Tafel slope, η is the overpotential, i is the current density, R is Avogadro's constant, T is the temperature, α is the cathodic charge transfer coefficient (α= 0.5) and F is Faraday constant.

For HER, the theoretical Tafel slopes are 120 mV dec^{-1}, 40 mV dec^{-1}, and 30 mV dec^{-1} corresponding to the Volmer-Heyrovsky step, the Heyrovsky step, and the Tafel step, respectively[2].

5.5 Coulombic Efficiency Measurement method of Coulombic Efficiency

$$CE=\frac{nQ_C+Q_S}{nQ_C+Q_T} \tag{5}$$

Where CE is Coulombic Efficiency, n is the number of cycles, Q_T is the initial deposition capacity, Q_C is the charging/discharging capacity and Q_S is the last stripping capacity[3].

6. Characterizations

The rotational rheometer (XGD, Discovery HR20) was used to measure the variation in the elastic and loss moduli of the PLSE-In electrolyte with frequency in plate mode. The tensile mechanical properties of the PLSE-In electrolyte were assessed using an electronic universal testing machine (UTM5105), following GB/T 528-1998 standards. The electrolyte's structure was analyzed with a Fourier transform infrared

(FTIR) spectrometer (Nicolet iS50), while Raman spectroscopy was performed using a WITec Alpha300R. The glass transition temperature (T_g) was determined using a high-pressure differential scanning calorimeter (HP DSC, 204HP). X-ray diffraction (XRD) patterns were obtained using a Tescan Clara GMH diffractometer with Cu-Kα radiation ($\lambda = 1.5418$ nm). X-ray photoelectron spectroscopy (XPS, PHI 5000 Versa Probe III) with an Al-Kα ray source was used to analyze the surface chemical composition of the Zn anode. Additionally, valence band spectra of the zinc foils were obtained using ultraviolet photoelectron spectroscopy (UPS) on samples from symmetric cells assembled with PLSE-In and run at a current of 0.5 $\mathrm{mA \cdot cm^{-2}}$. Morphologies of the Zn anode were examined with a field emission scanning electron microscope (FESEM, ZEISS Sigma 300) at an accelerating voltage of 10.0 kV. High-resolution transmission electron microscopy (HRTEM, Talos F200X) with an accelerating voltage of 200.0 kV was used to analyze the SEI. Time of Flight Secondary Ion Mass Spectrometry (TOF-SIMS, TOF-SIMS 5) was employed to detect the evolution of the In-rich SEI.

Hammett's acidity value (H_0) was measured with a UV spectrophotometer (UV2501PC, $\lambda = 500$ nm), using 7 M $ZnCl_2$ as the reference solution and methyl orange as the indicator for the blank sample (5 $\mathrm{mg\ L^{-1}}$).

Where the Hammett acidity value was calculated from the absorbance of the solution:

$$H_0 = (pKa)_{aq} + [\frac{A_n}{A} \Big/ (1 - \frac{A_n}{A})] \tag{6}$$

H_0 is the Hammett acidity value, pKa is the dissociation constant of the indicator, A is the absorbance of the blank sample, A_n is the absorbance of the sample to be measured. The relevant solutions are shown in **Fig. S6**[4, 5]. For PLSE-In and PLSE, we dispersed the solid electrolyte in a suitable non-polar solvent, ensuring that the acidic sites remain accessible to the indicator. This dispersion method has been shown in prior studies to yield a semi-quantitative assessment of surface acid strength that can be compared to liquid-phase measurements.

The Shirley background is subtracted from the measured UPS spectra. The position of the center of the valence band is given by:

$$E_d = \frac{\int N(\varepsilon)\varepsilon d\varepsilon}{\int N(\varepsilon)d\varepsilon} \tag{7}$$

where $N(\varepsilon)$ is the DOS or, in our case, the UPS-intensity after background subtraction. The background subtracted spectra were integrated up to 10.0 eV BE with respect to E_F, which is calculated from the Au film as a reference.

7. Theoretical calculations and simulations

7.1 Molecular dynamics

The geometry and energy optimization for polyacrylonitrile (PAN) were performed using the Vienna Ab Initio Simulation Package (VASP)[6]. A plane wave basis set with a cutoff of 400 eV was employed, based on density functional theory (DFT). The convergence criteria for energy and residual force were set to less than 10^{-5} eV and 0.05 eV/Å, respectively. Additional material calculations were conducted using Material Studio (MS) software. Structural models for PAN, $ZnCl_2$, water, $InCl_3$,

$(ZnCl_4)^{2-}$, and $[Zn(H_2O)_6]^{2+}$ were constructed using the “Build” module of MS and optimized in the “Dmol3” module with the same parameters **(Fig. S7)**[7].

The electrostatic potentials of PAN were derived from electron density and population analysis. Adsorption models for PAN-Zn and PAN-Cl were constructed and optimized in the “Dmol3” module, using the GGA-PBE exchange-correlation functional with a fine convergence tolerance. By analyzing the adsorption differences of Zn and chlorine on PAN, the dissociation ability of PAN for these species was evaluated.

The “Blends” module was used to obtain the Flory-Huggins parameter (χ), the energy distribution curve, and the $(ZnCl_4)^{2}$-PAN phase diagram, were obtained, which were used to assess the compatibility of the solvated structures $(ZnCl_4)^{2-}$ and $[Zn(H_2O)_6]^{2+}$ with PAN **(Fig. S8)**[8, 9, 10, 11].

The electrolyte model was constructed using the “Amorphous Cell” module, and structure optimization was performed in the “Forcite” module, with COMPASS II selected for the force field and other parameters set to default.

The radial distribution function (RDF) obtained by molecular dynamics is calculated by the following equation:

$$g(r) = \frac{Vn(r)}{N4\pi r^2 dr} \quad (8)$$

Where *g(r)* is the radial distribution function, *V* is the total volume, *n(r)* is the number of particles at a distance *r*, *N* is the total number of particles, π is the circumference ratio, *r* is the distance, and d_r is the differential of the distance. All distances are measured relative to the center particle. The number density ρ = N/V is defined, where a higher mass density corresponds to a higher number density. In this experiment, the mass densities used are 1.828 g·cm^{-3} for 30 m $ZnCl_2$ and 1.98 g·cm^{-3} for PLSE.

First, the solvation free energy and cohesion energy were calculated, and the solubility parameters ($\delta_D, \delta_P, \delta_H$) of $ZnCl_2$ were obtained (**Tab. S2**)[12]. The radial distribution function (RDF) of the configuration was then analyzed[13]. Next, the number of hydrogen bonds in the "amorphous cell box" was determined using the hydrogen bonding statistics script provided by the software. Concurrently, the electrostatic potentials of PAN were derived from electron density and population analysis.

In the "Dmol3" module, the exchange-correlation functional was set to GGA-BLYP, with convergence tolerance set to fine, and core treatment set to DFT Semi-core Pseudopotentials. Orbital properties were calculated to determine the LUMO and HOMO of each substance.

To investigate the reaction steps of Zn deposition and hydrogen emission on the surface of zinc foil, adsorption models for Zn (002)-H(Zn) and Zn (002)-In-H(Zn) were constructed. As the co-deposited Zn-In in PLSE was a mechanical mixture, indium nanoparticles (4 atoms) were used for the Zn (002)-In configuration. The model was constructed by cutting three layers of the (002) crystal face and fixing the bottom two layers. The projected density of states (PDOS) was obtained through energy band and density of states analysis, and the D-band center was calculated[14].

Adsorption configurations of Zn and hydrogen atoms on the Zn (002) and Zn (002)-In surfaces were studied by analyzing adsorption energies. The Gibbs free energy

(ΔG_{H*}) of hydrogen adsorption was calculated (details in **Tab. S7**). Transition states and barriers for Zn deposition were determined using the transition state search method[15].

7.2 Indium finite element analysis COMSOL

Finite element analysis was conducted using the electrochemistry module (EC) in COMSOL[16.] A two-dimensional "sandwich" cell was constructed with different electrolytes (30 m $ZnCl_2$ and PLSE-In). The cell dimensions were as follows: the Zn electrode was 0.2 µm thick, the concentrated electrolyte layer was 0.689 µm thick, and the triangular shape of the simulated crater had a length of 0.7 µm and a height of 0.07 µm. Conductivities for the 30 m $ZnCl_2$ aqueous electrolyte and PLSE-In were approximated as 2.2 $mS \cdot cm^{-1}$ and 1.5 $mS \cdot cm^{-1}$, respectively. The average current density was set to 0.5 $mA \cdot cm^{-2}$ (**Fig. S17**).

7.3 Thermodynamic calculation (Pourbaix diagram)

E-PH diagram of the Zn-H_2O system, the Zn-H_2O-Cl (30 m $ZnCl_2$) system and the Zn-H_2O-Cl (43 m $ZnCl_2$) system were plotted using the "E-PH" module in HSC chemistry 6. The basic components selected were Zn, ZnO, $Zn(OH)_2$, Cl(-a), Zn(+2a), $ZnCl_2$(a), ZnCl(+a), $ZnCl_3$(-a), ZnO(a)[17].

Fig. S1 The optical images of source material for PLSE-In.

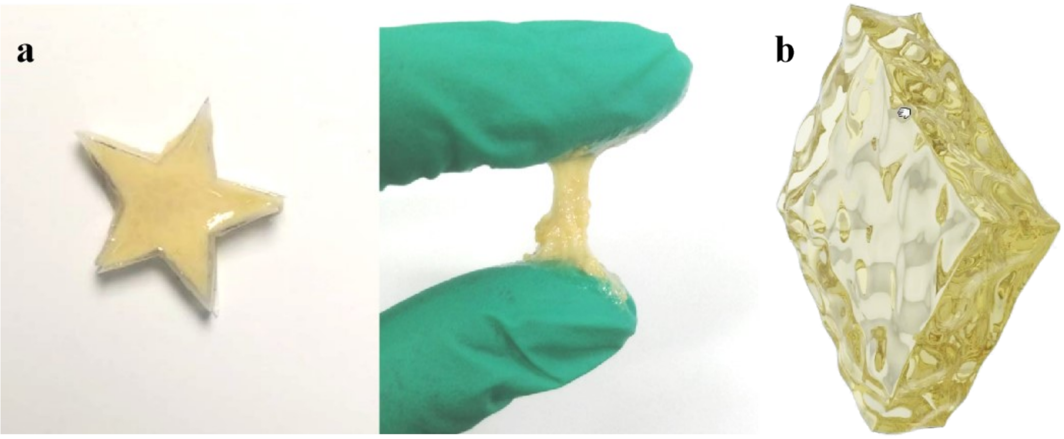

Fig. S2 (a) The optical images of PLSE-In on a slide taken from the mortar. (b) Schematic diagram of the normal gel.

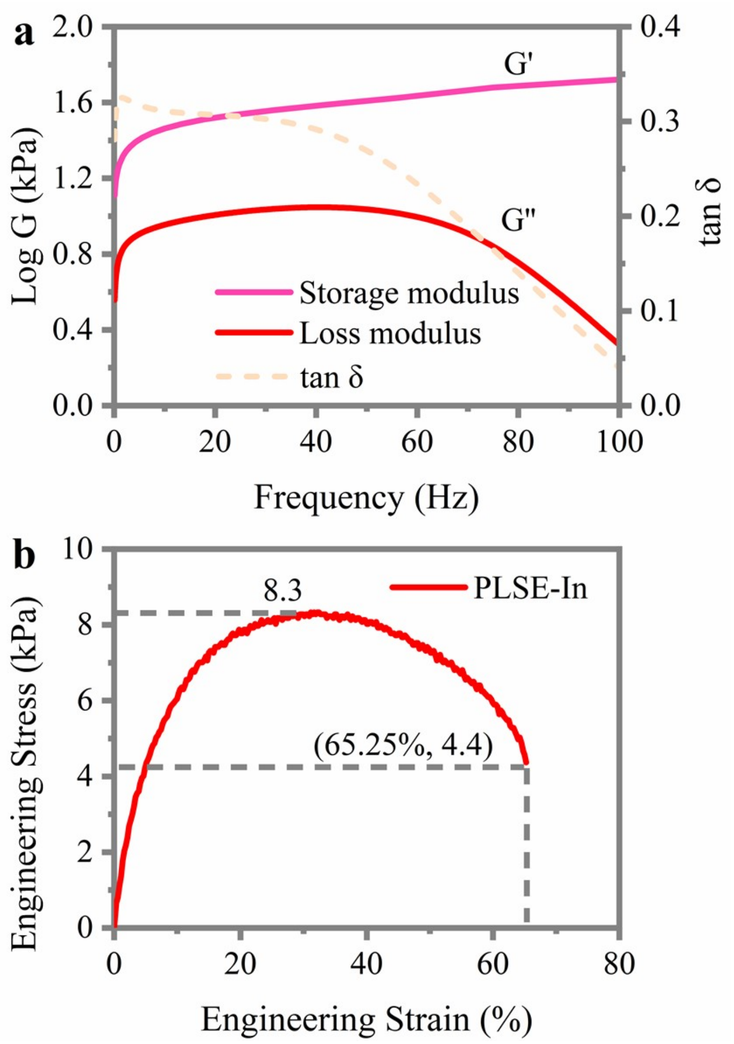

Fig. S3 (a) Rheological and (b) stress-strain curves of PLSE-In. The G′ and G″ represent storage modulus and loss modulus, respectively. G' measures the energy stored and recovered per cycle during deformation, reflecting the elastic (solid-like) properties of the material. Conversely, G" quantifies the energy dissipated as heat, indicating the viscous (liquid-like) characteristics.

Notes 1:

Within the 0.01-100 Hz frequency range, unlike gel electrolytes, the elastic modulus consistently exceeds the loss modulus, and the loss factor decreases with increasing frequency, indicating its strong solid-state behavior. The tensile test results show a maximum tensile strength of 8.3 kPa and an elongation at break of 65.25%, further supporting its viscoelastic properties similar to plasticine. Moreover, with a 14% (wt) water content and no free water present (as confirmed by radial function and Raman tests), along with notable differences in microstructure and macroscopic state compared to gels, jellies, and sols, we classify this material as “plasticine-like” solid electrolyte **(Fig. S2 and S3)**.

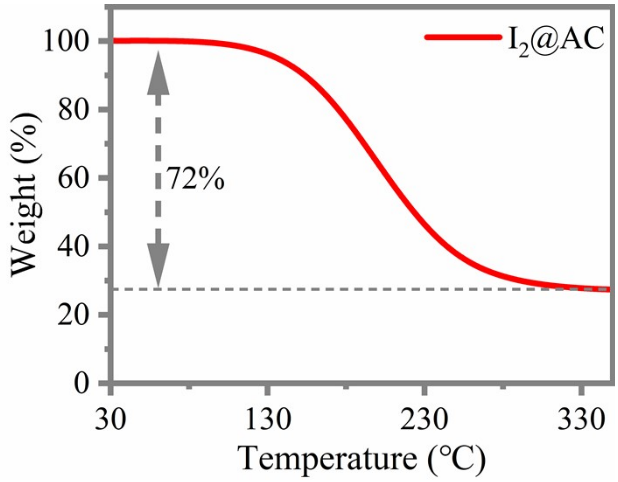

Fig. S4 Thermogravimetric curve of I_2@AC.

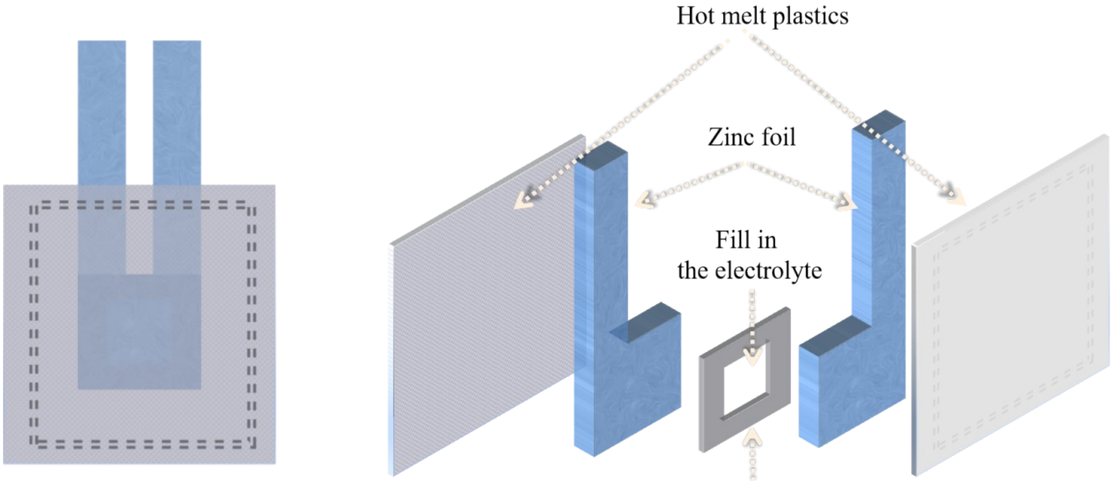

A spacer is made by digging a 1*1 cm^2 hole in the insulating material to support the electrolyte, preventing short circuits caused by crushing and deformation material.

Fig. S5 Schematic diagram of soft pack battery (left) and components (right).

Notes 2:

Despite the low water content and reduced acidity of PLSE, which contribute to lower corrosion risk, it is crucial to address the potential for corrosion of current collectors and cell cases. In practice, we utilized sealing and protective measures to prevent corrosion, ensuring the durability of the battery components. We assembled soft-pack batteries, as illustrated in **Fig. S5**.

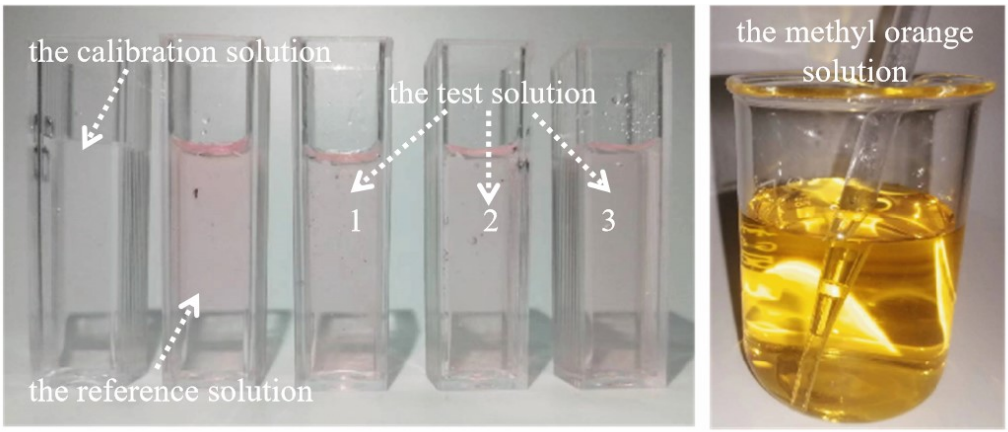

Fig. S6 The optical images of the calibration solution (H_2O), reference solution (7 m $ZnCl_2$, test solution (1:30m $ZnCl_2$, 2: PLSE and 3: PLSE-In) and methyl orange solution (5 mg·L^{-1}) prepared during the Hammett acidity value (H_0) test.

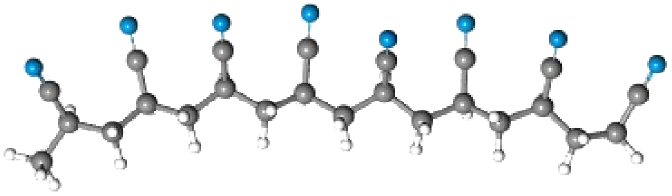

PAN

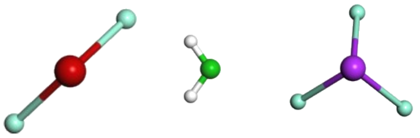

$ZnCl_2$, H_2O and InC

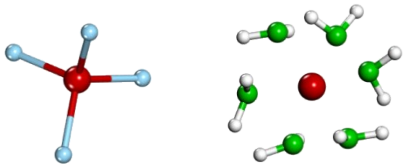

$(ZnCl_4)^{2-}$ and $[Zn(H_2O)_6$

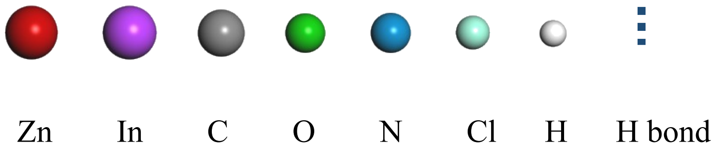

Fig. S7 The above are the molecular structures of polyacrylonitrile (PAN), Zinc chloride ($ZnCl_2$), water(H_2O), indium chloride($InCl_3$), zinc tetrachloride $(ZnCl_4)^{2-}$ and zinc hexahydrate $[Zn(H_2O)_6]^{2+}$, respectively.

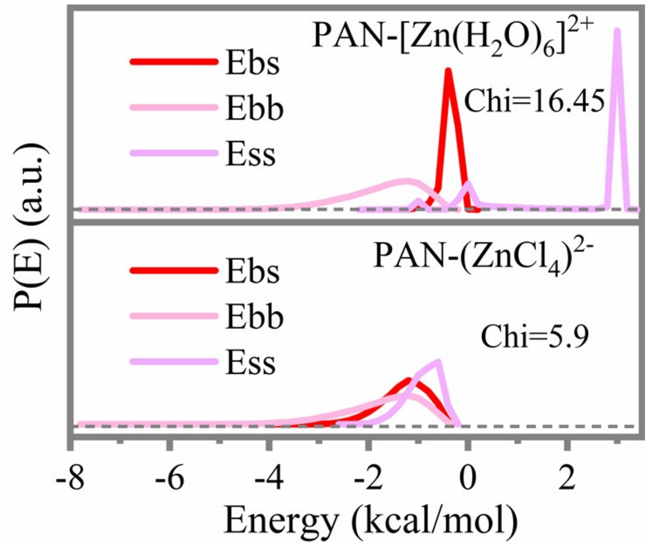

Fig. S8 Energy distribution curve (b:PAN, s: $[Zn(H_2O)_6]^{2+}/(ZnCl_4)^{2-}$). The Ebs (Binding Energy of Solvent) represents the interaction energy between the solvent molecules and the solute or electrode surface; The Ebb (Binding Energy of Bulk) denotes the cohesive energy within the bulk solvent or electrolyte, reflecting the internal interactions among solvent molecules.; The Ess (Surface-Solvent Interaction Energy) indicates the energy associated with the interaction between the electrode surface and the solvent molecules.

Notes 3:

The cohesive energy density of a mixture is calculated by subtracting the cohesive energy densities of the two pure substances from the total cohesive energy density. Cohesive energy density is defined as the energy required to vaporize the solvent into gas molecules.

The dimensionless Flory-Huggins parameter χ (chi) is commonly used to indicate the energy required for mixing: a positive χ ($\chi > 0$) signifies that heat is absorbed, while a negative χ indicates an exothermic process. Thus, the heat is absorbed, while the opposite is true for exotherm. Thus, a χ value of 0 or approaching 0 suggests good compatibility[8].

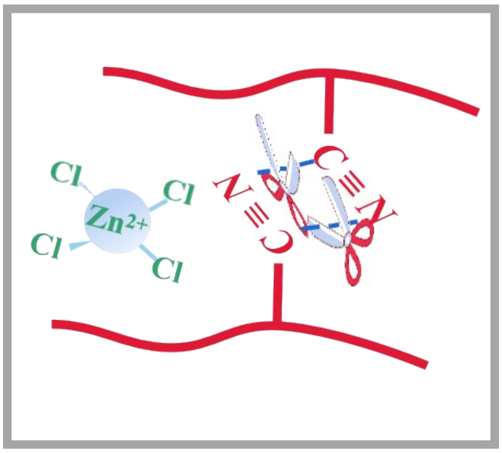

Fig. S9 Schematic diagram of $(ZnCl_4)^{2-}$ breaking the strong polarity of cyanoides between PAN chains[18, 19].

Tbl. S2 Hansen solubility parameters of the relevant raw materials in order to study the feasibility of PLSE-In

	δD	δP	δH	$(\delta D^2+\delta P^2+\delta H^2)^{0.5}$ $(\mathrm{J\ cm^{-3}})^{0.5}$	Clarification
H_2O	15.6	16	42.3	47.8	Handbook of chemicals
PAN	16	12.8	6.8	21.6	
$ZnCl_2$	- van der Waals	161.625 Electrostatic	4.616 Other	142.575	Calculated

The solubility of zinc chloride in water is equivalent to 432 g (100 g H_2O)$^{-1}$ (XXXpprox. 31m).

Notes 4:

The Hansen solubility parameter (HSP) divides the total cohesive energy density (E_T) into three components: dispersive (E_D), polar (E_p) and hydrogen bonding (E_H) contributions.

HSP values are derived by taking the square roots of the respective cohesive energy densities.

$$\delta = \sqrt{E} \tag{9}$$

When using solubility parameters, it is important to examine their similarity. The closer the solubility parameters are, the more compatible the substances are with each other[12].

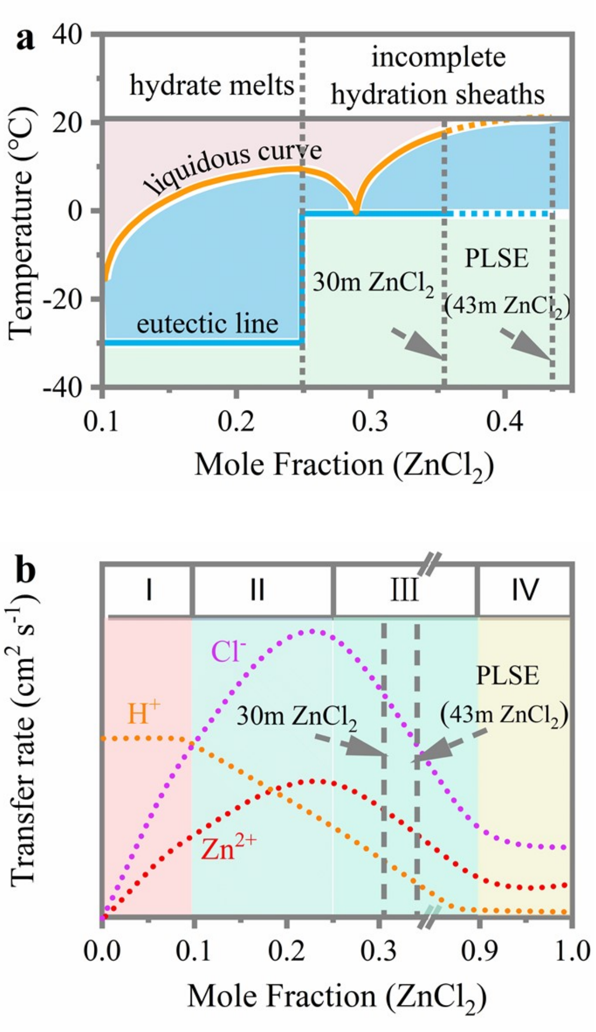

Fig. S10 (a) The H_2O-$ZnCl_2$ phase diagram is shown, where the yellow line represents the liquid phase line, the blue line indicates the eutectic line, and the dotted line connects the endpoints of the original phase diagram with the phase points from this work. For consistency in measuring the $ZnCl_2$ mole fraction, the PAN content was not considered in this plot, despite its presence in the work.

Notes 5:

From solvent sufficiency to solvent depletion, which produces solvation effects, the solution is presumably in one of the following conditions:

I. ideal dilute solution (<0.1);

II. II. solvated melt (0.1-0.25);

III. III. incompletely solvated sheath (0.25-0.9) and IV. pure substance (> 0.9)[20].

(1) Commonly used electrolytes typically fall within the range of ideal dilute solutions, while concentrated electrolytes are characterized by solvated melts or incomplete solvation layers. This work falls into the range of incomplete solvation layers, indicating a strong interaction between Zn^{2+}, Cl^-, and H_2O, which aligns with our solvation results. Additionally, in **Fig. S10a**, the concentrated electrolyte exhibits a liquid phase, a liquid eutectic mixed phase, and a eutectic phase as the temperature varies from 60°C to -40°C. The effect of temperature on the internal structure can be observed from the Arrhenius activation energy test; however, further investigation is needed to explore the microstructure at different temperatures.

(2) Using the Einstein-Nernst and Stocks-Einstein equations, we estimate the transport rate of each ion in the zinc chloride system to highlight the advantages of highly concentrated salts:

$$\sigma = \frac{nq^2}{6Pi\,\eta r} \tag{10}$$

Where σ is conductivity, *n* is the number of carriers per unit volume, *q* is the charge per carrier, *Pi* is π, η is solution viscosity and r is particle radius[21].

When the molar fraction of zinc chloride is less than 25%, the primary ionic species in solution is $[Zn(H_2O)_6]^{2+}$, which corresponds to the Raman peak at approximately. However, other species such as $(ZnCl)^+$, $ZnCl_2$, $(ZnCl_3)^-$, and $(ZnCl_4)^{2-}$ are also present, with their characteristic Raman peaks in the range of ~230-290 cm^{-1}. At a zinc chloride molar fraction of 25%, both $[Zn(H_2O)_6]^{2+}$ and $(ZnCl_4)^{2-}$ are the predominant ionic species. When the molar fraction exceeds 25%, $(ZnCl_4)^{2-}$ becomes the dominant species, and aggregates form through chloride ion sharing[20]. Overall, in this work, $(ZnCl_4)^{2-}$ is identified as the major ionic species.

Notes 6:

We can get the advantages of highly concentrated salt electrolytes:

(1) Higher Concentration as a Bridge to all-solid-State electrolytes: Highly concentrated salt electrolytes can serve as an intermediate step towards the development of all-solid-state electrolytes.

(2) Better Inhibition of Water Activity: These electrolytes reduce the transport rate of H^+ ions, thereby inhibiting water activity.

(3) Wider Electrochemical Window: Concentrated salt electrolytes offer a broader electrochemical window and reduce electrode solubility.

(4) Influence of PAN on Ionic Interactions: PAN, as a crucial component, affects the interaction between Zn^{2+} and Cl^-. It facilitates $ZnCl_2$ decomposition and enhances ionic mobility by adsorbing Cl^- and repelling Zn^{2+}. This improves the role of Zn^{2+} ions within the electrolyte, minimizes interference from other ions, and promotes effective zinc ion deposition.

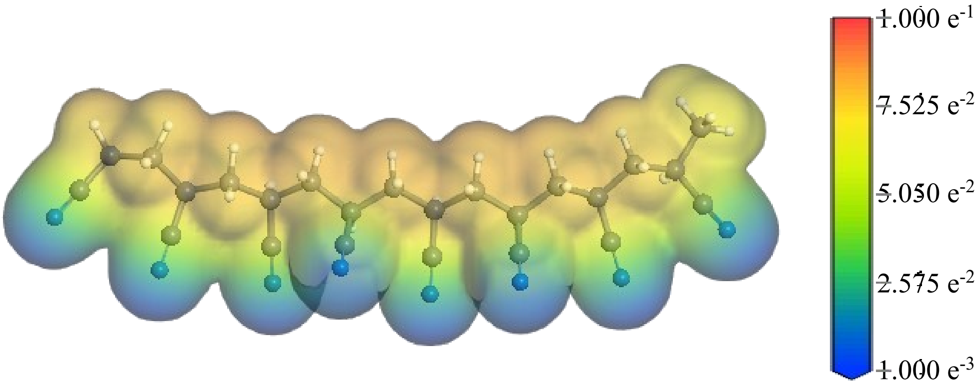

Fig. S11 The electrostatic potential diagrams of polyacrylonitrile (PAN) (above).

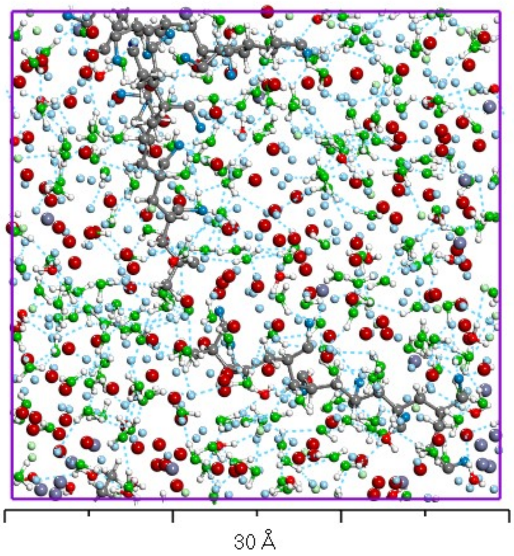

Fig. S12 Simulated molecular dynamics snapshot of PAN-$ZnCl_2$.

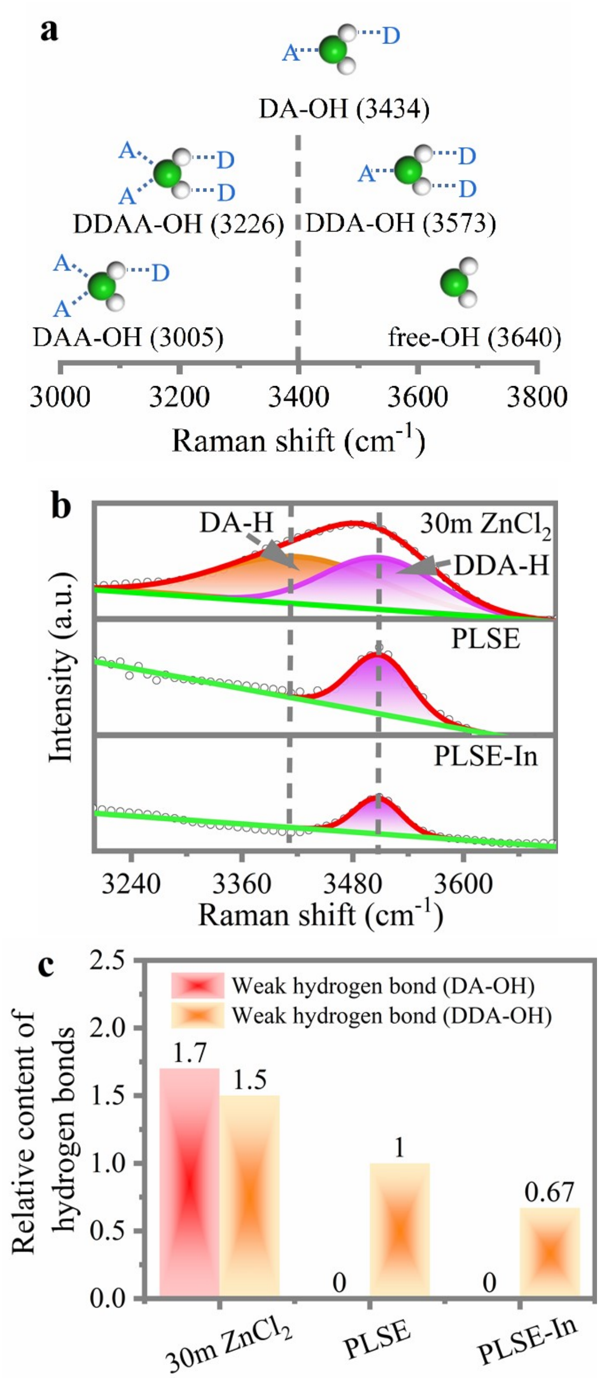

Fig. S13 Raman spectra of the different electrolytes and the associated interpretations: (a) Types of hydrogen bonding at different peak positions, (b) Raman spectra, and (c) Relative content of hydrogen bonds (the weak hydrogen bond (DDA-OH) content of PLSE is regarded as 1)[20].

Notes 7:

Fig. S13a illustrates the types of hydrogen bonds between water molecules, categorized as DDAA (double donor-double acceptor), DAA (single donor-double acceptor), DDA (double donor-single acceptor), DA (single donor-single acceptor), and free O-H vibrations. Strong hydrogen bonding is characterized by peaks below ~3400 cm^{-1}, while weak hydrogen bonding appears above this threshold.

According to **Fig. S13b** and **Fig. S13c**, highly concentrated electrolytes neither exhibit strong hydrogen bonds nor show significant free water molecules. As the salt content increases, the proportion of stronger coordination states, such as contact ion pairs (CIP) or aggregates (AGG), rises. Simultaneously, the available space for free water molecules decreases, confining the limited number of water molecules to incomplete coordination structures.

Notes8:

Hammett acidity estimation

In the ultra-high concentration electrolyte system, the reduced water content decreases the Hammett acidity. The solvated structures of chloride/cyanide and Zn^{2+} convert the electrolyte into a weaker proton donor. Additionally, the weak hydrogen bonding of the residual water reflects a diminished interaction between water and its environment, confirming the reduction in electrolyte acidity.

Moreover, we further illustrate this by assessing the intensity of electron gain/loss for Lewis's acids:

The Global Electrophilicity Index (GEI), denoted as ω, quantifies a molecule's ability to accept electrons. Introduced by Parr and colleagues in 1999, it is defined as:

$$\omega = \frac{\mu^2}{2\eta} \tag{11}$$

where μ is the chemical potential and η is the chemical hardness. The GEI is estimated using the following equation [22]:

$$\mu = \frac{E_{HOMO} + E_{LUMO}}{2} \tag{12}$$

$$\eta = E_{LUMO} - E_{HOMO} \tag{13}$$

Tbl. S3 ω estimation

	LUMO	HOMO	μ	η	ω
PLSE-In $(ZnCl_4)^{2-}$	-1.28	-6.72	-4	5.44	1.47
PAN	-0.8	-7.7	-4.25	6.9	1.30

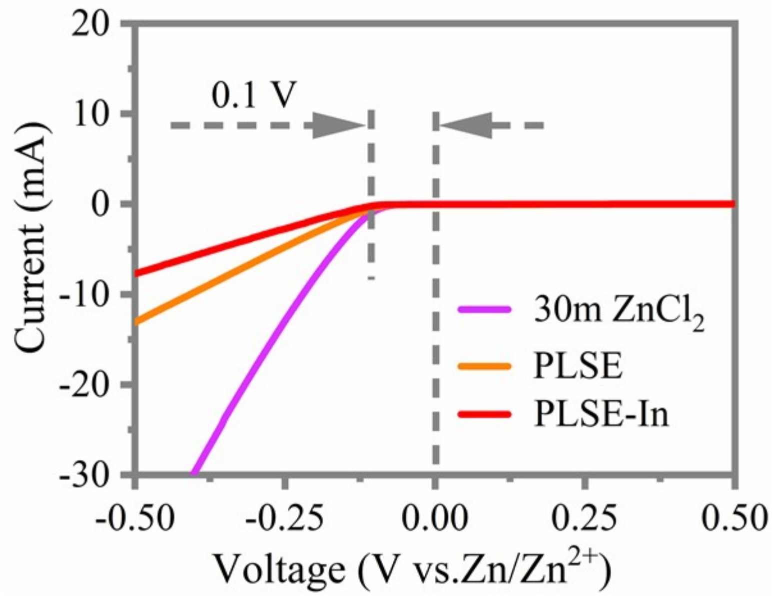

Fig. S14 Reduction side of electrochemical stabilization window test curve (LSV).

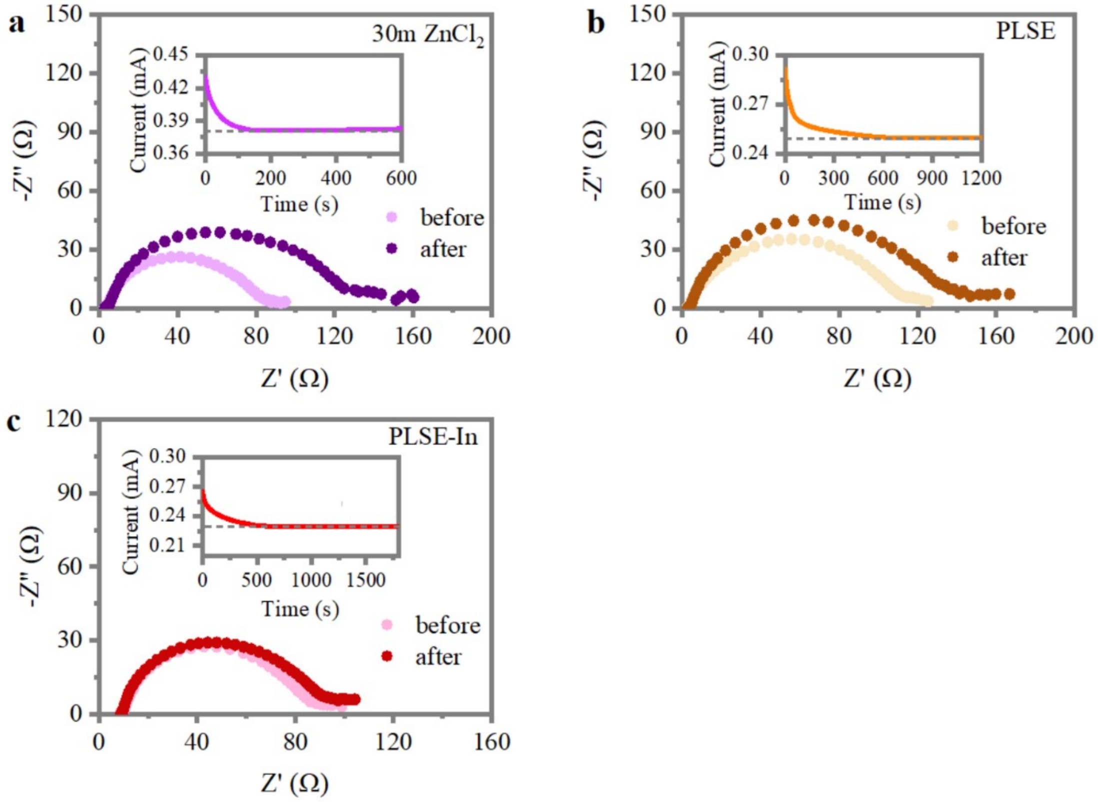

Fig. S15 Impedance spectrum of different electrolytes and the inset is the I-t curve (ΔV=10 mV) for measuring the Zn^{2+} ion transfer number.

Tab. S4 Relevant parameters used in the calculation of ionic conductivity and ion transfer number

Electrolyte	ΔV (mV)	I_0 (mA)	I_{ss} (mA)	R_0 (Ω)	R_{ss} (Ω)	R (Ω)	**t_+**	**σ(mS cm^{-1})**
30m $ZnCl_2$	10	0.43	0.38	12.1	7.76	21	0.6	2.2
PLSE	10	0.28	0.22	3.19	3.68	26	0.78	1.8
PLSE-In	10	0.26	0.23	0.85	1.47	30	0.9	1.5

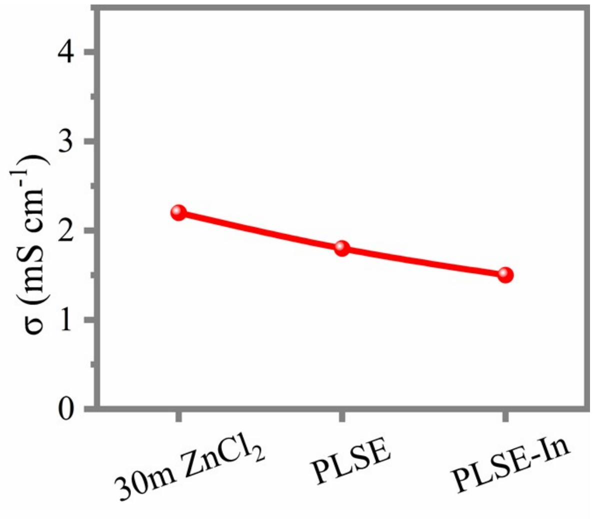

Fig. S16 The ionic conductivity of 30 m ZnCl^2, PLSE and PLSE-In.

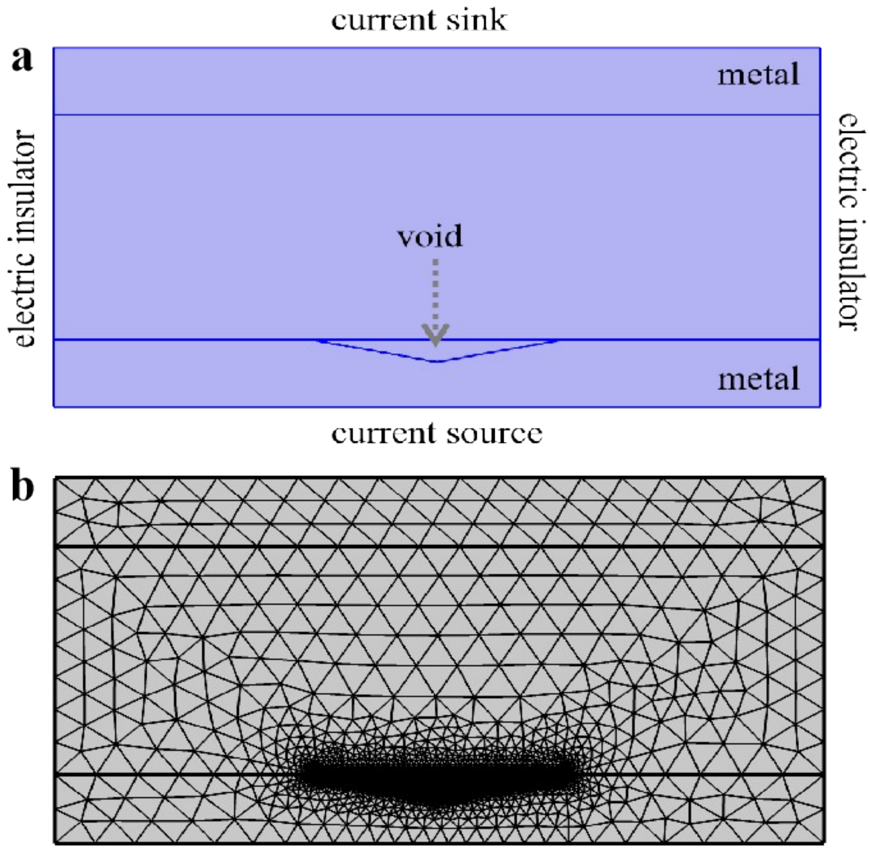

Fig. S17 (a) A geometric model used to simulate the distribution of electric field and dendrite growth in the vicinity of the void. In the model, the bottom Zn and top Zn are set as high voltage and ground, respectively. The left and right boundaries are set as electrically insulating. Triangular voids are used to simulate circular pits; (b) Mesh division of the above 2D model.

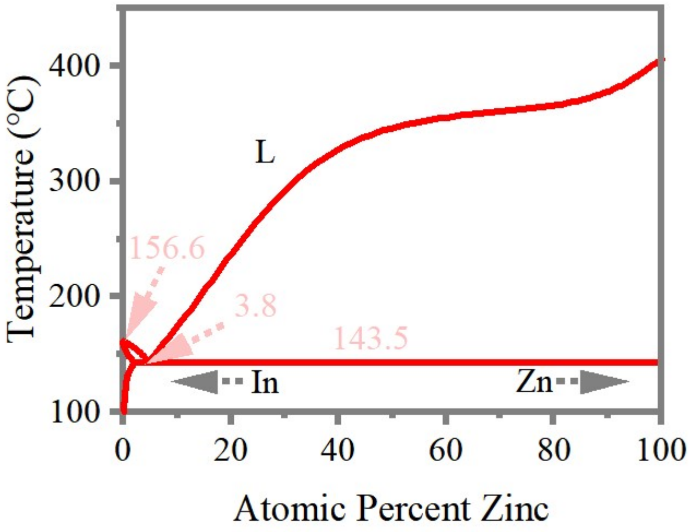

Fig. S18 Phase diagrams of Zn with indium.

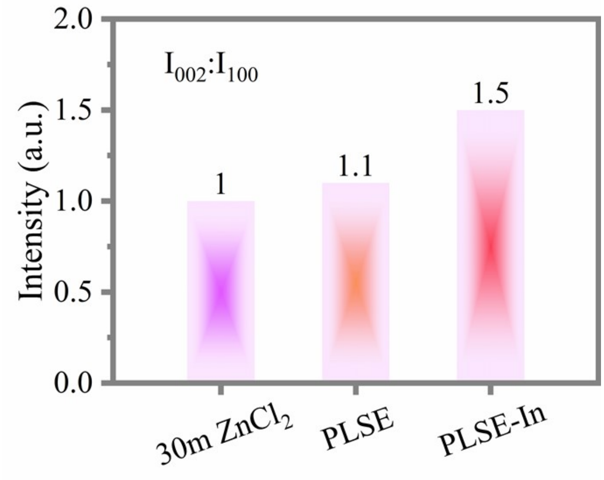

Fig. S19 The ratio of (002)/(001) peak intensity after 20 hours cycling test at 1 mA·cm^{-1}, 0.5 mAh·cm^{-1}.

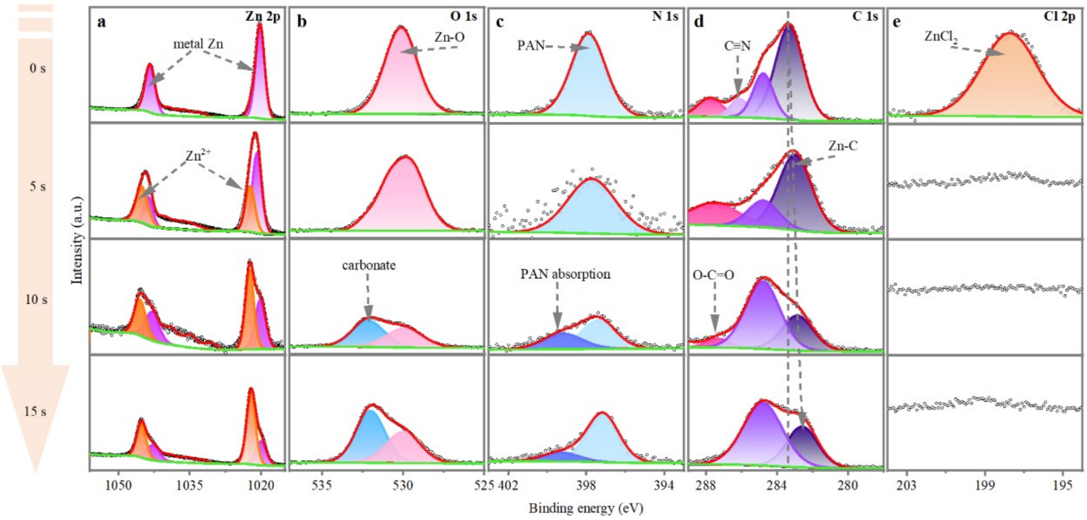

Fig. S20 High-resolution of XPS spectra for Zn 2*p* (a), O 1*s* (b), N 1*s* (c), C 1*s* (d) and Cl 2*p* (e) and under different etching times from 0 to 15 s.

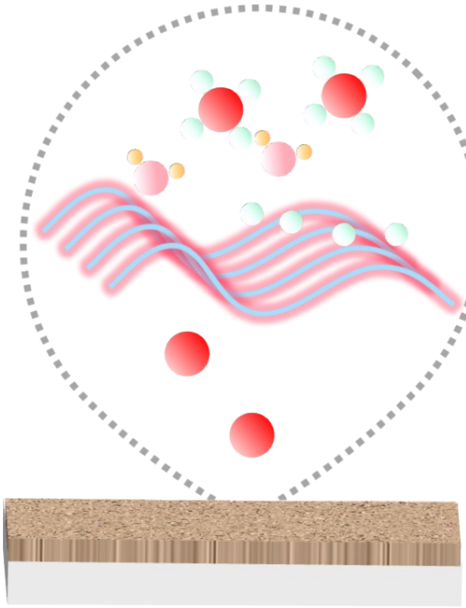

Fig. S21 Schematic diagram of the role of PAN in the composite solid-state electrolyte interphase.

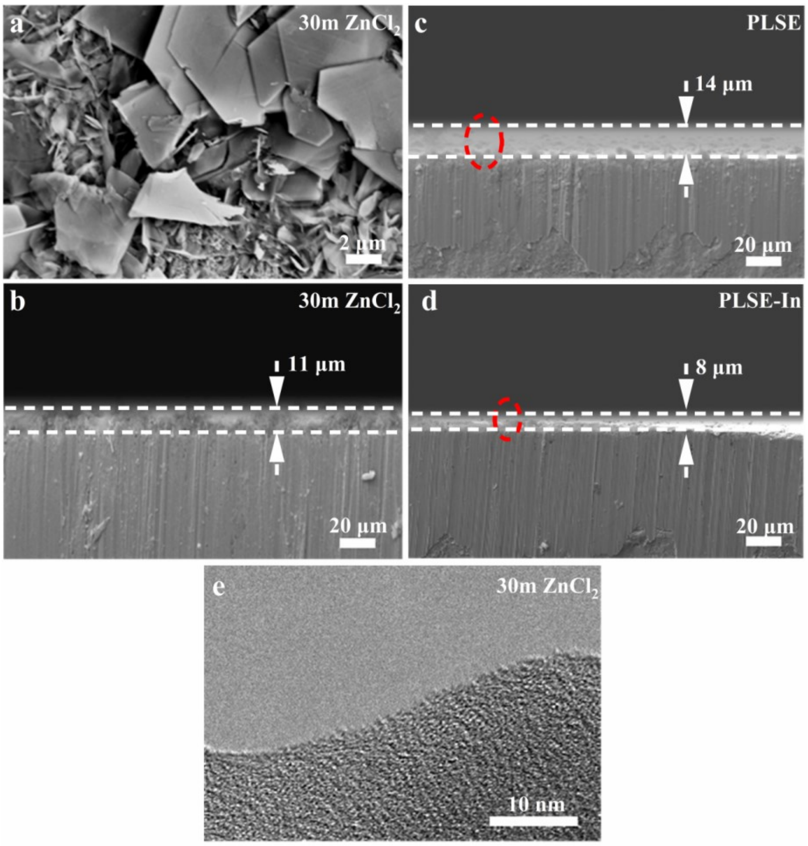

Fig. S22 Morphology characterization of Zn anode after the charge/discharge cycles: (a) SEM images and (b) corresponding cross-section image of Zn foil surface of 30 m $ZnCl_2$ aqueous electrolyte, respectively, where the red circle marks the position at higher resolution. Cross-section images of (c) PLSE and (d) PLSE-In. All samples were cycled for 50 hours at 0.5 mA·cm^{-1}, 0.25 mAh·cm^{-1}. (e) TEM images of the edge of copper grid points from a Zn||Cu battery assembled with 30 m $ZnCl_2$ aqueous electrolyte after cycling for 20 hours at 0.5 mA·cm^{-1}and 0.25 mAh·cm^{-1}.

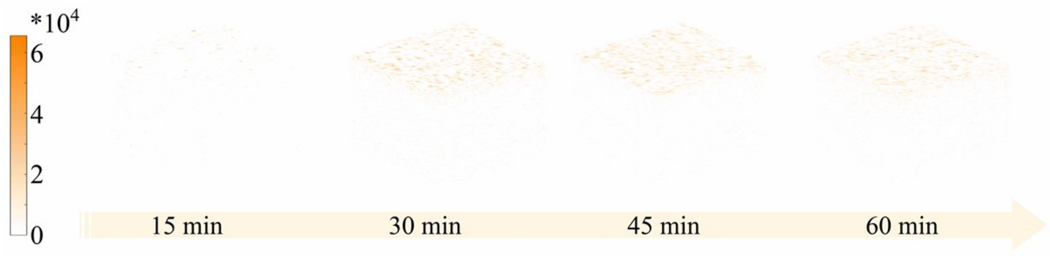

Fig. S23 Three-dimensional image data of Zn elements on the surface of the Zn foil were obtained under charging and discharging conditions (1 mA·cm^{-1}, 0.5 mAh·cm^{-1}) for symmetric batteries using Time-of-Flight Secondary Ion Mass Spectrometry (TOF-SIMS). These images provide detailed spatial distribution and depth profiling of Zn on the electrode surface, revealing insights into the elemental redistribution during electrochemical cycling.

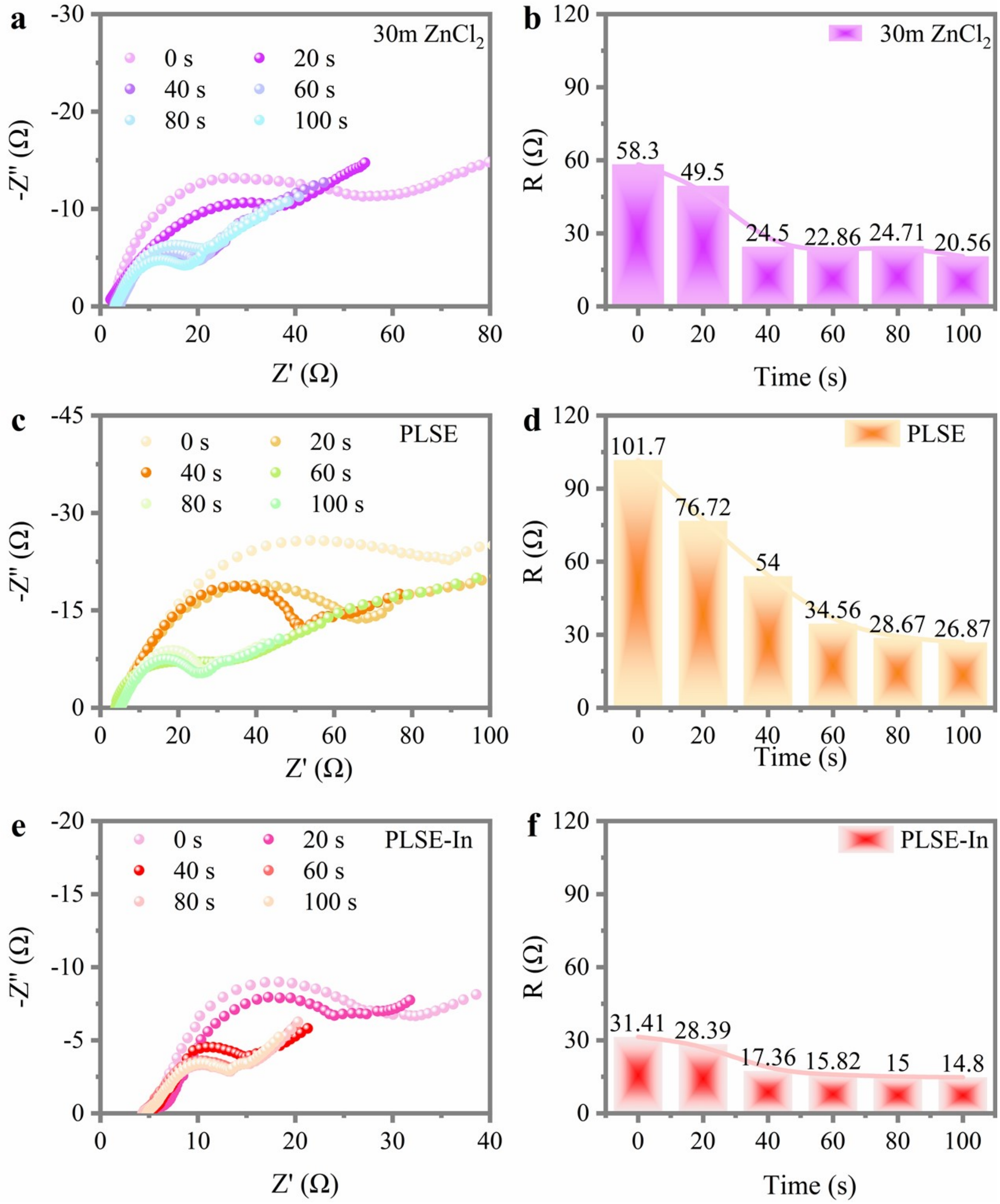

Fig. S24 Electrochemical impedance spectra (EIS) of symmetric cells were recorded at different time intervals (0 s, 20 s, 40 s, 60 s, 80 s, and 100 s) during charging. The spectra were obtained for cells assembled with (a) 30 m $ZnCl_2$, (c) PLSE and (e) PLSE-In. Corresponding impedance plots for (b) 30 m $ZnCl_2$, (d) PLSE and (f) PLSE-In displayed the evolution of the impedance response.

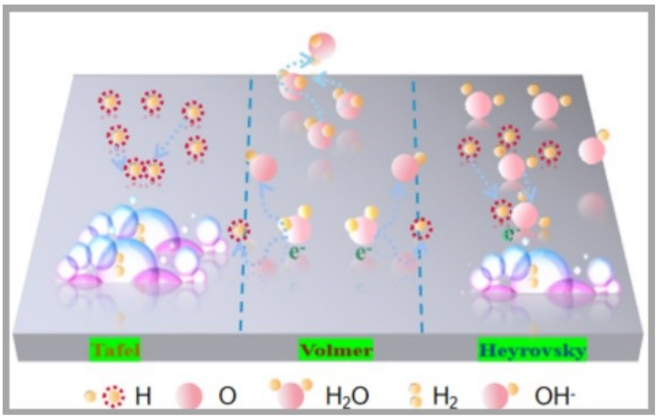

Fig. S25 Schematic of hydrogen emission reaction (HER).

Notes 9:

Under acidic conditions, the hydrogen evolution reaction (HER) can follow two distinct pathways: the Volmer–Heyrovsky process or the Volmer–Tafel process.

Volmer: $H_3O^+ + e^- + * \rightarrow H^* + H_2O$

Heyrovsky: $H^* + H_3O^+ + e^- \rightarrow H^2 + H_2O + *$

Tafe: $2H^* \rightarrow H_2 + 2*$

where H* represents the adsorbed hydrogen atom and * represents the active site for hydrogen adsorption.

The first step in the process, known as the Volmer reaction, involves the reduction and adsorption of hydrogen ions on the electrode surface through single-electron transfer. The second step, referred to as either the Heyrovsky or Tafel reaction, occurs when the adsorbed hydrogen atom combines with another hydrogen atom to form an H_2 molecule, which then desorbs from the electrode surface.

In HER, the rate-determining step (RDS) can be estimated using the Tafel slope:

If the Volmer reaction is the RDS, the Tafel slope is approximately 118 mV·dec^{-1}.

If the Heyrovsky or Tafel reaction is the RDS, the Tafel slope is around mV·dec^{-1} and 29.5 mV·dec^{-1}, respectively.

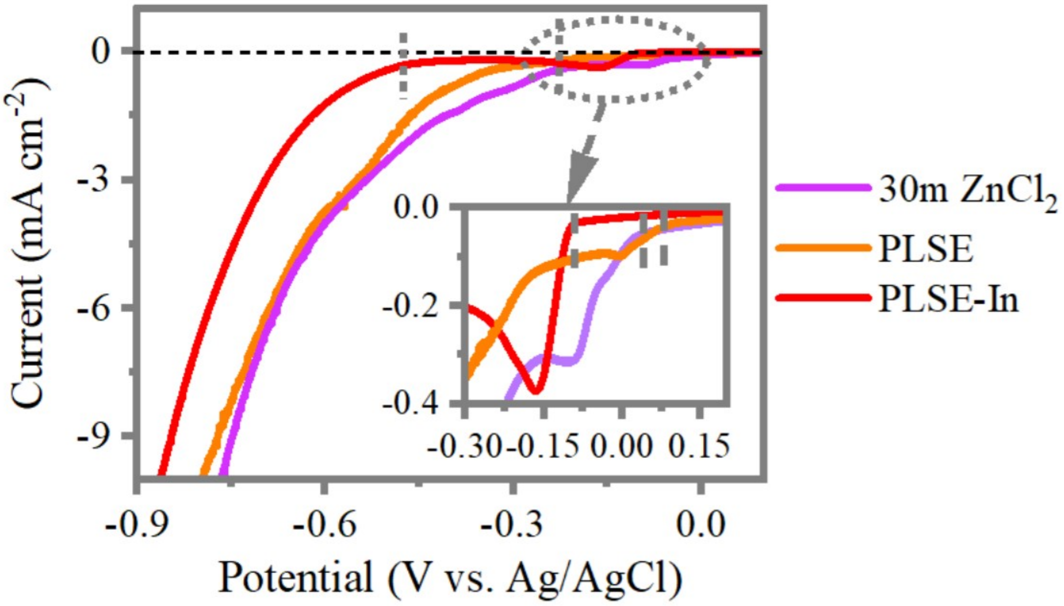

Fig. S26 LSV curves of hydrogen evolution reaction (HER).

Tab. S5 D-band centers calculated from UPS curves.

Time (s)	Ed (eV)
0	-6.876
20	-7.998
40	-8.014
80	-8.024
100	-8.028

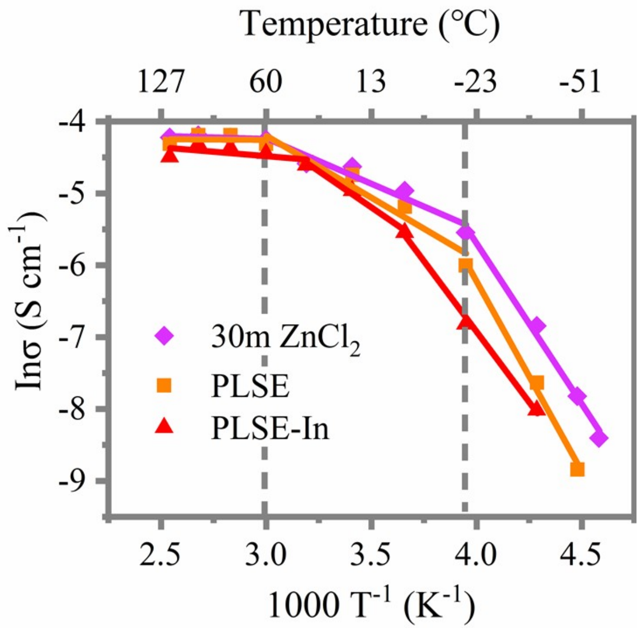

Fig. S27 The lines obtained by fitting Arrhenius formula for 30 m $ZnCl_2$ aqueous electrolyte, PLSE and PLSE-In.

Tab. S6 Activation energy of 30 m $ZnCl_2$, PLSE and PLSE-In at different temperature range.

Electrolyte	**Temperature (℃)**	**Activation energy (eV)**
30 m $ZnCl_2$	-55~-20	0.39
	-20~60	0.11
	above 60	0.002
PLSE	-50~-20	0.46
	-20~60	0.15
	above 60	0.007
PLSE-In	-40~0	0.34
	0~40	0.17
	above 40	0.02

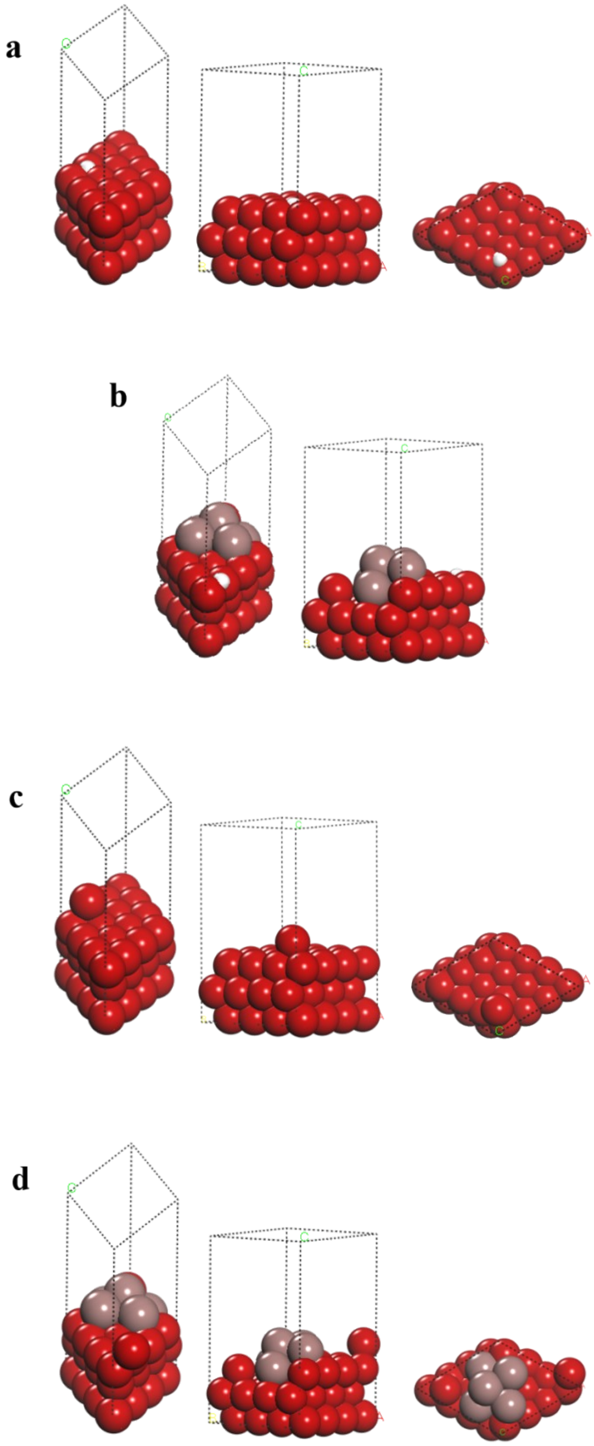

Fig. S28 H adsorption configurations on (a) Zn and (b) Zn-In, respectively. The Zn adsorption configurations on (c) Zn and (d Zn-In, respectively.

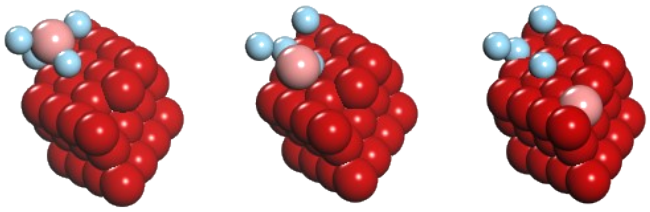

Fig. S29 Transition state search: reactants, transition states and products during crystallization of Zn^{2+} ions on the Zn-In structure.

Tbl. S7 Calculation results of the free energy for HER on Zn and Zn-In under different electrolytes.

	Reaction coordinate	E+ZPE (eV)	TS (eV)	G (eV)	ΔG (eV)
PLSE (Zn)	$*+H^++e^-$	/	/	/	0
	H^*	-1.7	3.21	-4.91	0.38
	$*+1/2H_2$	-1.88	3.41	-5.29	0
PLSE-In (Zn-In)	$*+H^++e^-$	/	/	/	0
	H^*	-2.7	5.57	-8.27	-0.5
	$*+1/2H_2$	-2	5.77	-7.77	0

Notes 10:

The free energy of hydrogen adsorption at equilibrium is calculated as followings:

$$G = E + ZPE - TS$$

$$\Delta \mathrm{G} = G_{H^*} - G_{*+1/2H_2}$$

Where the* represents an active site and H* represents hydrogen adsorption in the active site. Since $G_{total(*+H++e-)}$=$G_{total(*+1/2H2)}$, just calculating $G_{total(*+1/2H2)}$, the ZPE (denotes the zero-point vibrational energy) is included in E+ZPE. Considering the small vibrational entropy of H*, all the corrections are put together to take 0.2 eV[15, 23].

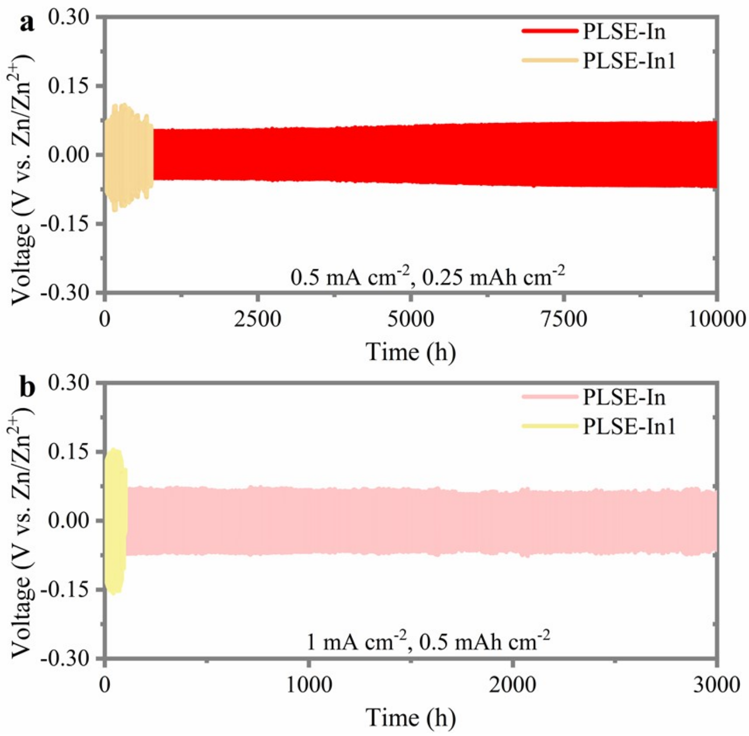

Fig. S30 The cycling performance of Zn‖Zn symmetrical batteries assembled by the PLSE-In and PLSE-In$_1$ (Relatively high indium content) under (a) 0.5 mA·cm^{-2}, 0.25 mAh·cm^{-2} and (b) 1 mA·cm^{-2}, 0.5 mAh·cm^{-2}.

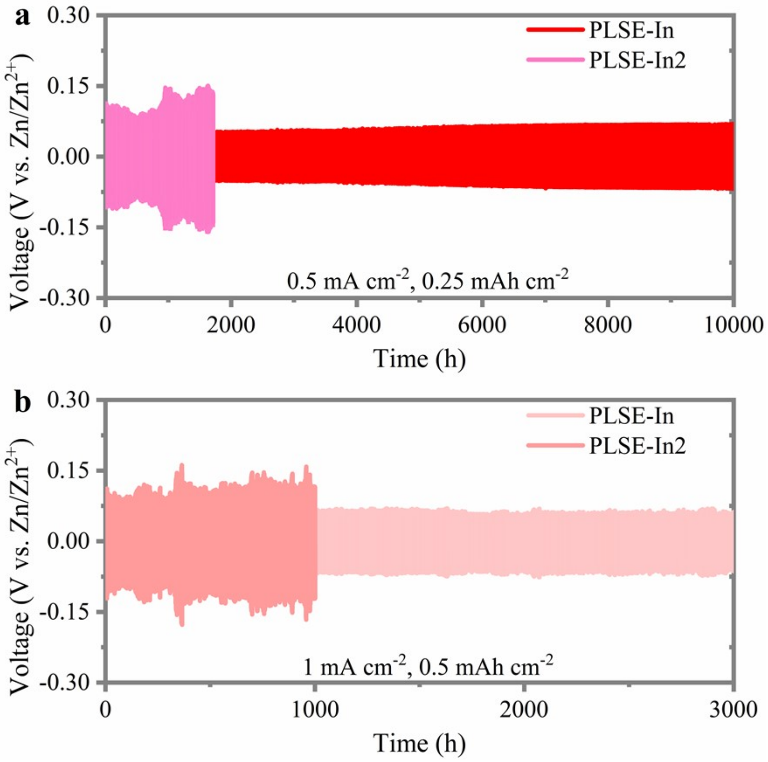

Fig. S31 The cyclic stability of Zn‖Zn symmetrical batteries assembled by the PLSE-In and PLSE-In$_2$ (relatively high PAN content) under (a) 0.5 mA·cm^{-2}, 0.25 mAh·cm^{-2} and (b) 1 mA·cm^{-2}, 0.5 mAh·cm^{-2}.

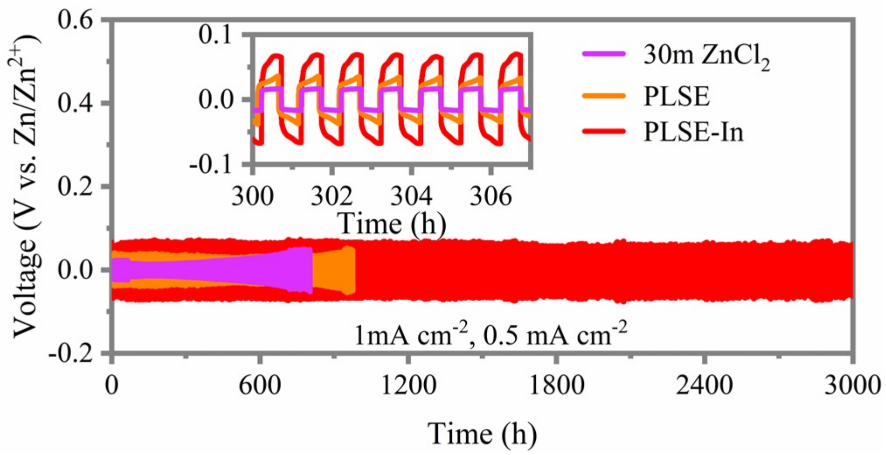

Fig. S32 The cycling performance of Zn||Zn symmetrical batteries assembled by the different electrolytes under 1 mA·cm^{-2}, 0.5 mAh·cm^{-2}.

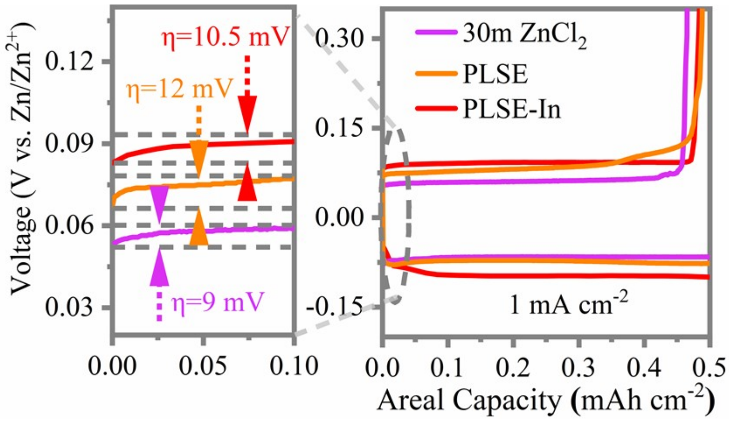

Fig. S33 Corresponding charge/discharge polarization curves of Zn Cu batteries (the enlarged plot is on the left).

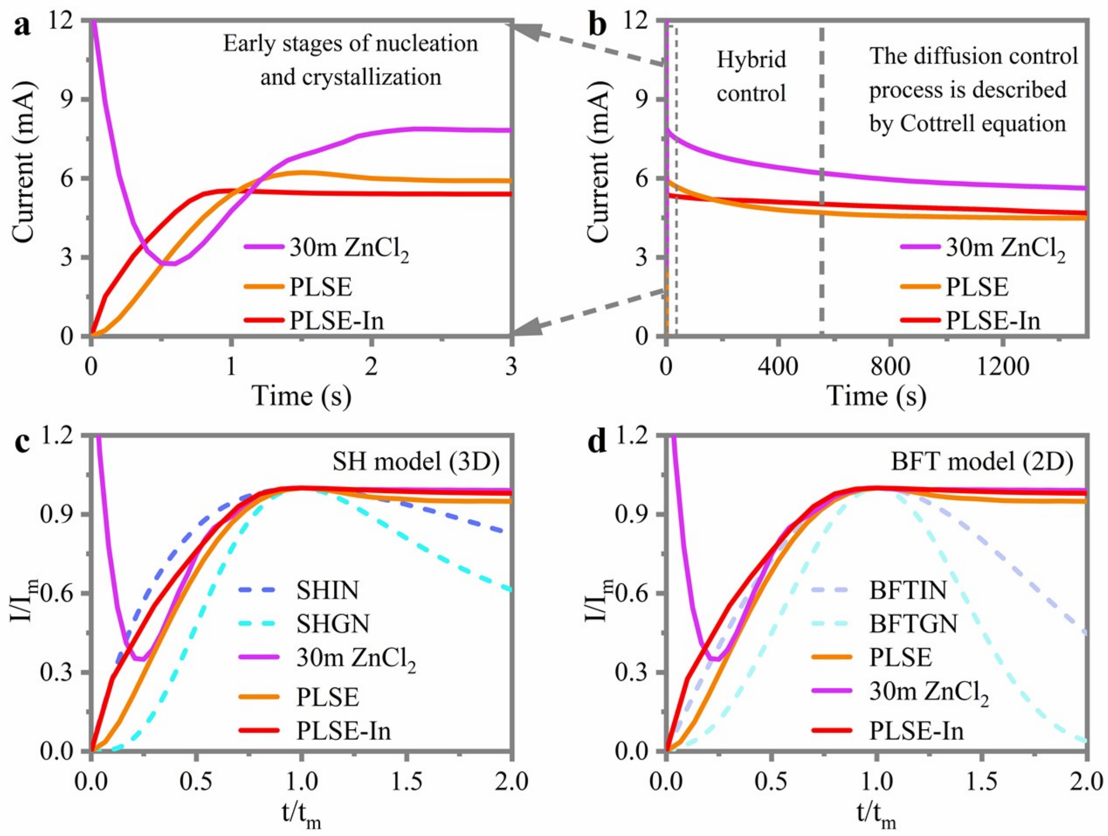

Fig. S34 I-t curve analysis of different electrolytes (the loading voltage is 150 mV): (a) enlarged view of early nucleation and crystallization; (b) I-t curve analysis of different electrolytes; (c) I-t factorless curve (model of Scharifker and Hill's three-dimensional hemispherical crystal nucleus, SH model); and (d) I-t factorless curve (model of Bewick, Fleshmann and Thirsk's two-dimensional disk-shaped crystal nucleus, BFT model).

Notes 11:

Analytical method of chronograph current curves (I-t)

1. Early stages of nucleation and crystallization

(1) Scharifker and Hills (SH) developed a model based on the assumption that

randomly distributed hemispherical nuclei on the electrode grow under 3D diffusion control. When growth centers overlap, they derived dimensionless equations for two nucleation scenarios:

Instantaneous nucleation (SHIN)

$$(I/I_m)^2 = \frac{1.9542\{1 - \exp[-1.2564(t/t_m)]\}^2}{t/t_m} \tag{14}$$

Progressive nucleation (SHGN)

$$(I/I_m)^2 = \frac{1.2254\{1 - \exp[-2.3367(t/t_m)^2]\}^2}{t/t_m} \tag{15}$$

(2) Bewick, Fleissman, and Thirsk (BFT) developed a model assuming that randomly distributed disk-shaped nuclei on the electrode grow under 2D diffusion control. Similar to Scharifker and Hills, when growth centers overlap, the dimensionless equations are provided for two nucleation scenarios:

Instantaneous nucleation (BFTIN)

$$I/I_m = \exp\{-\frac{1}{2}[(t/t_m)^2 - 1]\}t/t_m \tag{16}$$

Progressive nucleation (BFTGN)

$$I/I_m = \exp\{-\frac{2}{3}[(t/t_m)^3 - 1]\}(t/t_m)^2 \tag{17}$$

Where *I* is current, t is polarization time, I_m and t_m are the maximum current and the corresponding time, respectively[24].

2. The diffusion control process is described by Cottrell equation:

$$I = \frac{nFSD^{\frac{1}{2}}C_0}{(\mathrm{Pit})^{\frac{1}{2}}} \tag{18}$$

Where *I* represent current, t is polarization time, *n* is electron transfer number of electrode reaction, *F* is Faraday constant, *S* is electrode area, *D* is diffusion coefficient of conductive ions, C_0 is initial molar concentration of conductive ions, and *Pi* is π.

The curve can be divided into three main stages: the initial nucleation and growth phase, the mixing control phase, and the bulk-phase diffusion control phase. Since the Scharifker-Hills and Bewick-Fleissman-Thirsk models are derived under ideal conditions, the curves do not perfectly align in practice due to factors such as interfacial atom diffusion, desolvation behavior, ion diffusion in the bulk phase, and side reactions. As a result, the second half of the curves show deviations. In the early part of the bulk-phase diffusion control region, we recognize a hybrid control phase.

The bulk-phase diffusion control process follows the Cottrell equation, which indicates that the current is proportional to the diffusion coefficient. From this, we can infer that the diffusion coefficient of 30 m $ZnCl_2$ is slightly higher than that of PLSE and PLSE-In, which is consistent with previous analyses (**Fig. S34b**).

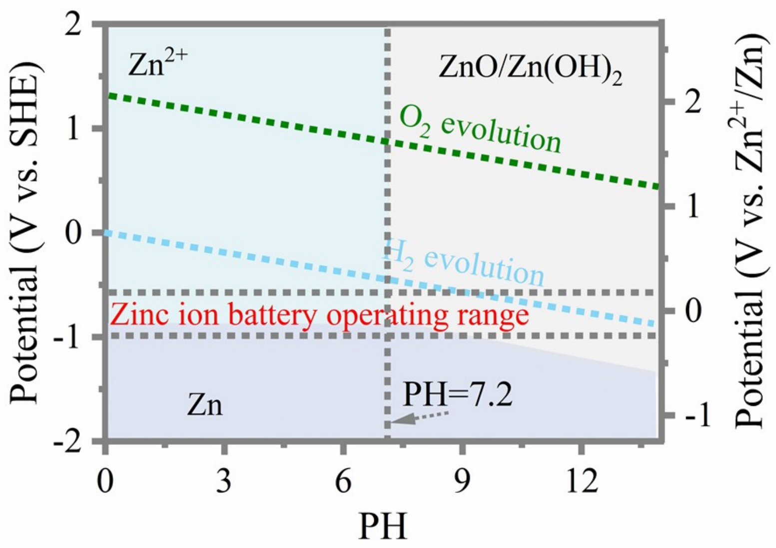

、**Fig. S35** Pourbaix diagram of Zn-H_2O system.

Notes 12:

Potential-pH diagrams illustrate the thermodynamically stable regions of different species in a solution at varying potentials (E) and pH levels. The stability region of water is marked by a thick dashed line, while the Zn ion anode operation region is indicated by a thin line. Horizontal lines reflect electron-dependent but pH-independent reactions, while vertical lines indicate pH-dependent but electron-independent reactions. Diagonal lines represent reactions influenced by both electrons and pH[17].

Due to the complex interactions of microscopic particles, only the most abundant and dominant species are shown. In the Zn-H_2O-Cl system with 30 m $ZnCl_2$ aqueous electrolyte and PLSE-In, the stabilization regions of Zn^{2+} are likely dominated by $ZnCl_2$(a) and $ZnCl_3$(a-), with potential contributions from $(ZnCl_xH_2O_y)_{2-x}$ complexes. This corresponds with earlier discussions on solvation structure, where increased $ZnCl_2$ leads to more chloride involvement in complexation, displacing the hydrated structure seen in dilute solutions.

Despite no significant change in the stabilization regions between the 30 m $ZnCl_2$ Zn-H_2O-Cl and PLSE (43 m $ZnCl_2$) Zn-H_2O-Cl systems, this is likely due to the idealized nature of the model. Comparing the $Zn^{2+} \rightarrow ZnO$ reaction lines in the Zn-$H_{22}O$-Cl system (pH 7.8) with those in the Zn-H_2O system (pH 7.2) suggests that concentrated $ZnCl_2$ systems are more suited to acidic conditions, though the advantage of dilute solutions is minimal.

While this analysis doesn't show a clear advantage for PLSE (43 m $ZnCl_2$) over 30 m $ZnCl_2$, PLSE (43 m $ZnCl_2$) offers competitive benefits in corrosion inhibition and reducing side reactions. Under acidic conditions, the dissolution of zinc into zinc ions, along with complexation with water molecules and anions, remains key to both zinc corrosion and side reactions[25].

Corrosion:

$$Zn+2H^+ \rightarrow Zn^{2+}+H_2\uparrow \tag{17}$$

Side reaction:

$$Zn^{2+}+OH^-+ZnCl_2+xH_2O \rightarrow [ZnCl_2(OH)]^- \cdot xH_2O \tag{18}$$

Despite its acidity, the highly concentrated salt system significantly reduces corrosion due to the presence of an indium-rich composite solid-state electrolyte interphase (In-rich SEI). This system exhibits minimal side reactions, even though localized high pH can lead to the formation of $[ZnCl_2(OH)]^- \cdot xH_2O$, which remains soluble in the acidic electrolyte. Consequently, passivation layers are difficult to form under mild and acidic conditions, whereas they are more readily produced under alkaline conditions.

Tab. S8-1 Comparison of performance parameters of related the electrolytes.

Electrolyte		t_+	Ionic conductivity (mS cm^{-1})	Voltage stability window (V)	Running time of symmetrical battery (h)	Current density (mA cm^{-2})	Supplemental instruction	Reference	
electro-lytes	10 m Zn(OAc)$_2$/KOAc	0.42	/	2.5	1200	0.5	*0.5 mAh*	*Nat. Sustainability*	26
	30 m ZnCl$_2$/TFE	/	17.75	2.8	4500	0.2		*PNAS*	27
	30 m ZnCl$_2$/chloride salt/DMC	/	/	/	/	0.2	*volatile*	*Nat. Sustainability*	28
	30 m ZnCl$_2$ Wise	/	/	2.3	600	0.2		*Chem. Commun.*	3
	75 m ZnCl$_2$/ZnBr$_2$/Zn(OAc)$_2$	/	1.28	/	/	/	*-40-80* °C	Adv. Mater.	13
	Zn$_x$K$_{(1-x)}$(OAc)$_{(1+x)}$	/	/	/	1200	1		*Energy Environ. Sci.*	29
	Zn(AATZ)$_2$ PSIC	0.94	0.9	3	2000	0.2	*0.2 mAh*	*Adv. Mater.*	30
	Zn(OAc)$_2$/PAN	0.8	0.018	4.6	/	/	*Zinc-air*	*Matter*	31
	4 m ZnSO$_4$/CMC	/	/	/	5800	5	*5 mAh*	*Adv. Mater.*	32
	PEO/CuF$_2$	0.42	/	/	200	0.1	Li$^+$	*Adv. Energy Mater.*	33
	Li$_2$ZnCl$_4$•9H$_2$O	/	100	/	/	/	-60~80 °C	*Nat. Sustainability*	34
	42 m LiTFSI + 21 m Me$_3$EtN·TFSI	/	0.91	3.25	/	/	Li$^+$	*ACS Energy Lett.*	35
	20 m KCF$_3$SO$_3$/30 mKFSI	/	4.34	3	/	/		*ChemElectroChem*	36
	ZnSO$_4$/Ni $^{2+}$	/	/	/	900	1		*Angew.Chem.Int.Ed.*	37
PLSE-In (43 m ZnCl$_2$)		0.9	1.5	6.8	10000	0.5		***This work***	

Tab. S8-2 Comparison of performance parameters of related the electrolytes.

Electrolyte		**t_+**	**Ionic conductivity (mS cm^{-1})**	**Voltage stability window (V)**	**Running time of symmetrical battery (h)**	**Current density (mA cm^{-2})**	**Supplemental instruction**	**Reference**	
Zn-In	Zn@In	**suppression of HER （$ZnSO_4$ and $InCl_3$）**			9000		Chemical replacement	*Energy Environ. Sci.*	23
	Zn|In foils	**corrosion inhibitor, nucleating agent, and suppress corrosion（$ZnSO_4$ and $InCl_3$）**			1500		Chemical replacement	*Small*	38
	Ga-In-Sn-Zn solid-liquid composite anode	**good adsorbing ability and lower migration energy barrier ($InSn_4$)**			600	/	/	*Energy Storage Mater.*	39
	$ZnIn_3$@In-Zn	**high Zn affinity and high hydrogen evolution overpotential**			10000	/	Chemical replacement	*Energy Storage Mater.*	40
	Zn|ITO	**p-Band Centers**			4000	/		*Angew.Chem.Int.Ed.*	41
	Zn|$In_{0.2}Sn_{0.8}$	**adsorption energy and high hydrogen evolution overpotential**			1800	/	Chemical replacement	*Adv. Funct. Mater.*	42
	InZn alloy anodes	**well-dispersed zinc domains surrounding indium domains**			700 Unstable operation		electrodeposition	*ACS Energy Lett.*	43
	GaIn@Zn	**evolution overpotential and improved corrosion**			2100			*ACS Energy Lett.*	44
	Zn@In&ZnF_2	**Hydrogen evolution inhibition**			1400			*ACS Appl. Mater. Interfaces*	45
	$Zn(OTf)_2$/ 0.3 m $In(OTf)_3$	**adsorption energy nuclear induction**			5700 Unstable operation	2	In-situ	*Adv. Funct. Mater.*	46
PLSE-In ($43\ m\ ZnCl_2$)		0.9	1.5	6.8	10000	0.5		***This work***	

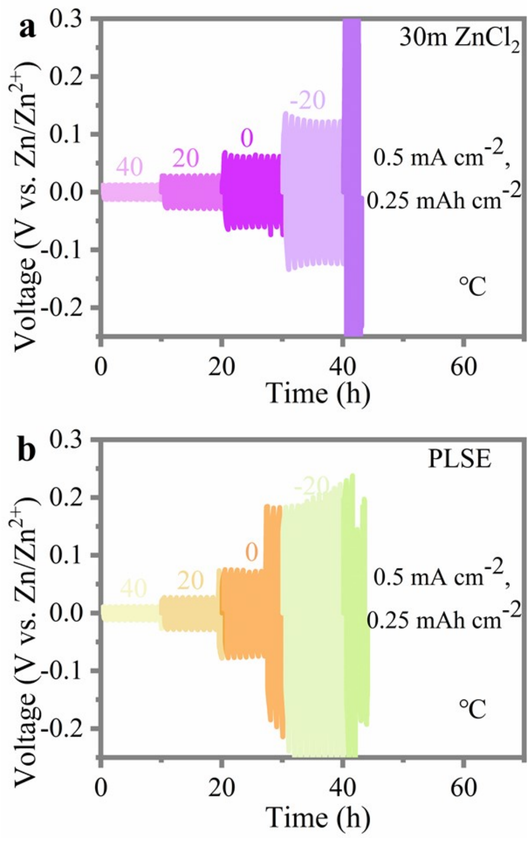

Fig. S36 Cycling test under different temperature conditions.

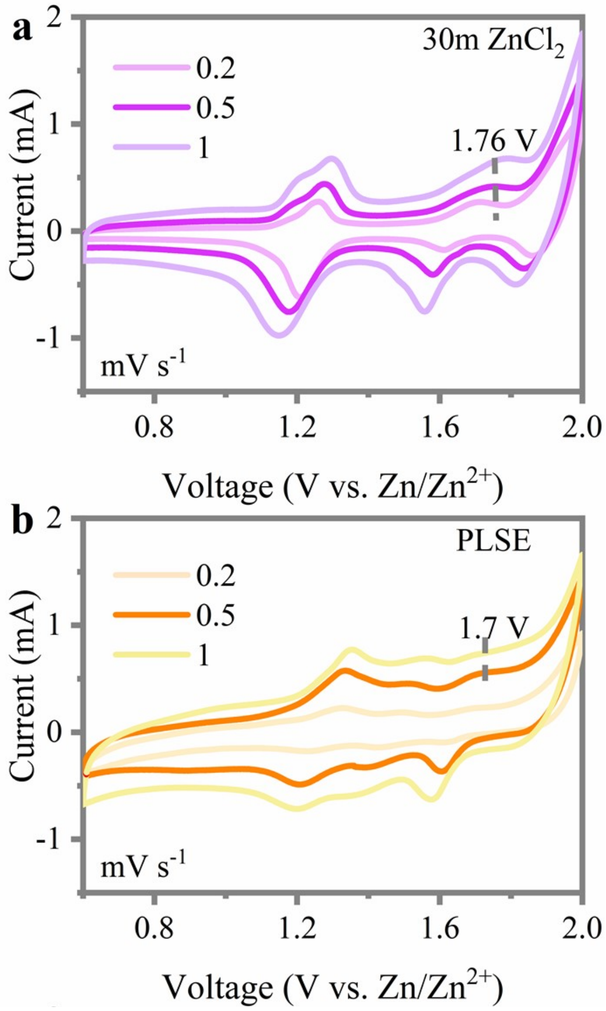

Fig. S37 CV curves of Zn‖I$_2$ batteries with the 30 m ZnCl$_2$ and PLSE at scanning rate of 0.2, 0.5 and 1 mV s^{-1}.

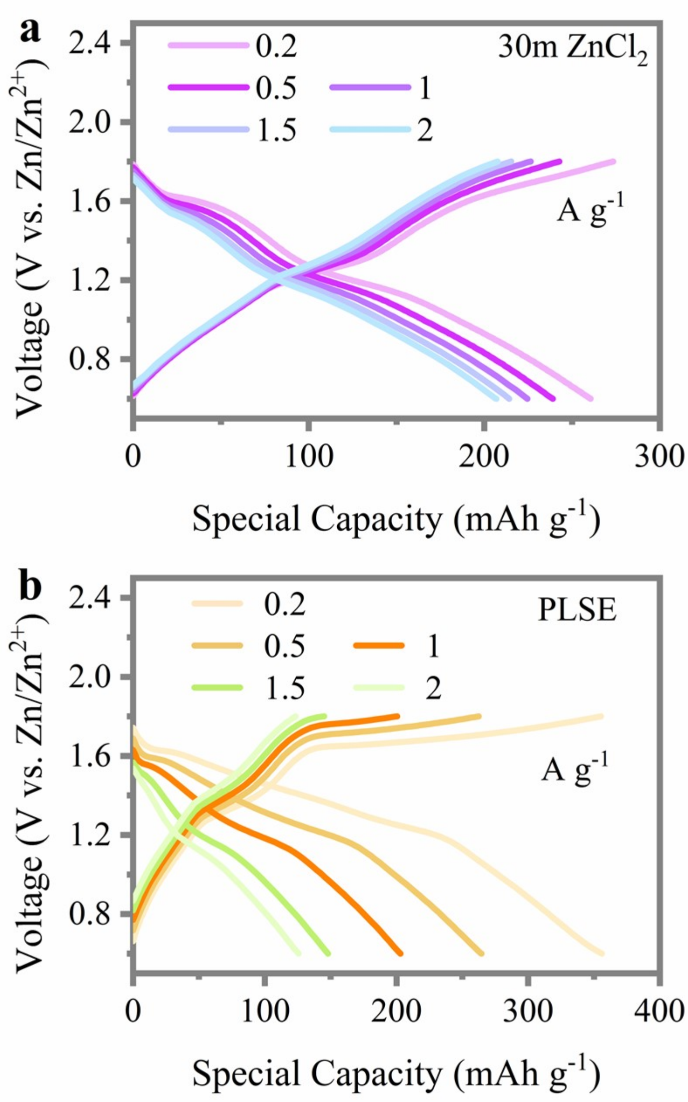

Fig. S38 GCD curves of Zn||I$_2$ batteries with the 30 m ZnCl$_2$ and PLSE.

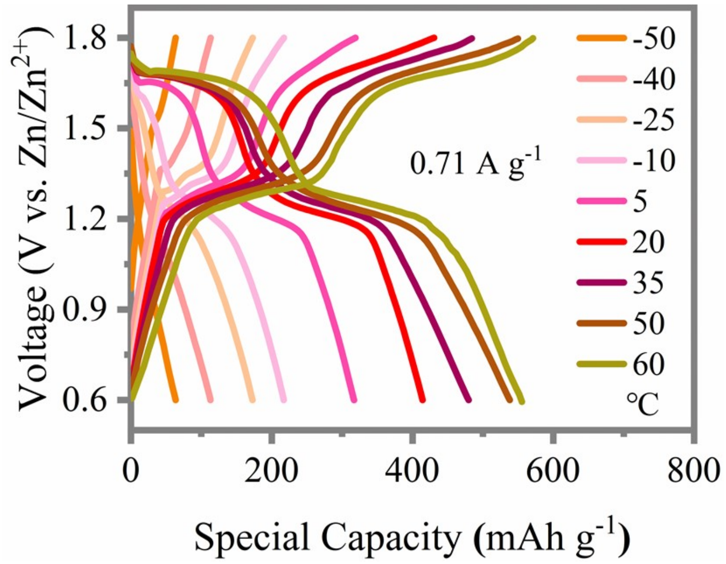

Fig. S39 GCD curves of Zn||I_2 batteries with the PLSE-In at different temperatures.

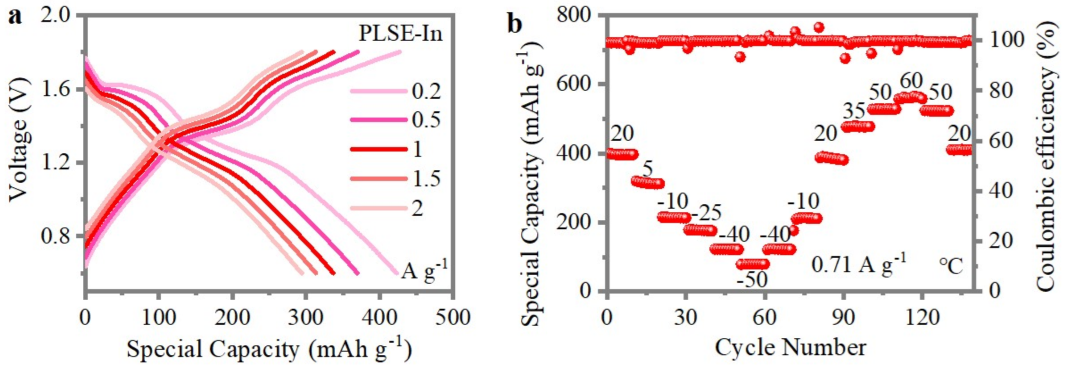

Fig. S40 (a) GCD curves of batteries with PLSE-In at different current densities of 0.2, 0.5, 1, 1.5 and 2 A g^{-1}; (b) Electrochemical performance of Zn I_2 batteries with PLSE-In at temperatures from -50 °C to 60 °C.

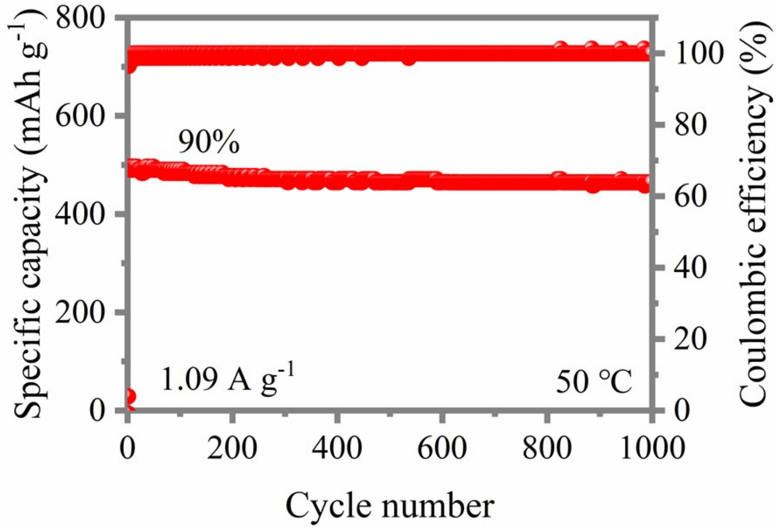

Fig. S41 Cyclic stability of Zn||I_2 batteries with PLSE-In at high temperature.

Notes 13:

Chloride ions can excite iodine positive ions, leading to a high specific capacity through a four-electron transfer. We investigated the performance of different electrolytes in Zn||I_2 batteries. The CV curves for the Zn||I_2 cell with three different electrolytes all show two pairs of redox peaks, corresponding to the redox reactions of I^-/I_0 (1.4 V) and I_0/I^+ (1.79 V) couples, respectively[47].

The batteries with PLSE-In exhibit a larger integration area and more consistent peaks, indicating fewer side reactions and better reversibility (**Fig. S37 and 40a**). Due to the high transfer number of PLSE-In and the protective In-rich SEI, the Zn||I_2 full cell demonstrates excellent rate capability. When the charge/discharge current density is increased from 0.2 to 2 A·g^{-1}, the specific capacity declines moderately from 450 to 358 mAh·g^{-1} and recovers to 450 mAh·g^{-1}, maintaining a Coulombic efficiency of over 98% throughout the process. In comparison, batteries with PLSE and 30 m $ZnCl_2$

aqueous electrolyte show initial capacities of 420 mAh·g^{-1} and 360 mAh·g^{-1} at 0.2 A·g^{-1}, respectively, but only 145 mAh·g^{-1} and 254 mAh·g^{-1} at 2 A·g^{-1}, which are significantly lower than those with PLSE-In (**Fig. S38, S39**,**S40b and c**).

With dendrite-free Zn stripping/plating and a water-poor environment, the Zn||I_2 battery with PLSE-In demonstrates ultra-long stability over 1200 cycles at 1 A·g^{-1}, retaining 89.28% of its initial capacity with nearly 100% Coulombic efficiency. In contrast, the battery with PLSE fluctuates at a lower capacity of 270 mAh·g^{-1} at the same current density, while the cell with 30 m $ZnCl_2$ shows a capacity decay to 150 mAh·g^{-1} after only 400 cycles (**Fig. S40d**).

To assess environmental adaptability, we tested Zn||I_2 batteries at temperatures ranging from -50 to 60°C. Batteries with PLSE-In show a steady capacity increase from 80 mAh·g^{-1} at -50 °C to 566 mAh·g^{-1} at 60°C at a current density of 0.7 A·g^{-1} (Fig. S39e and S40). Additionally, at 50 °C and 1 A·g^{-1}, the Zn||I_2 battery delivers a high capacity of 483 mAh·g^{-1} and achieves stable cycling for 1,000 cycles with 90% of the initial capacity retained **(Fig. S40 e and S41)**.

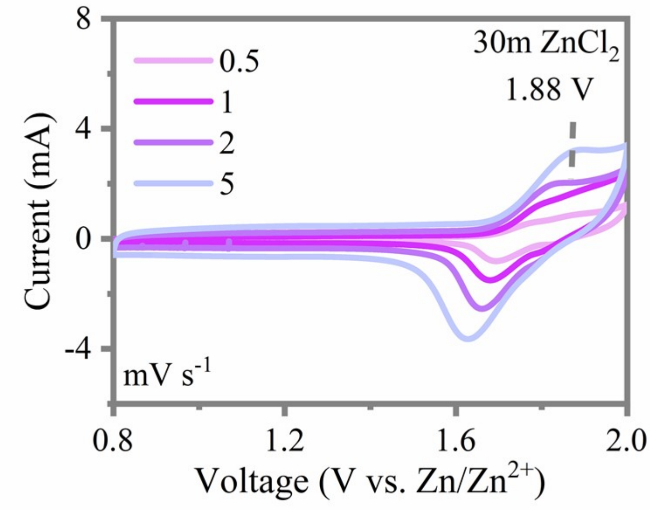

Fig. S42 CV curves of Zn‖Br$_2$ assembled with 30 m ZnCl$_2$ at scanning rate of 0.5, 1, 2 and 5 mV·s^{-1}.

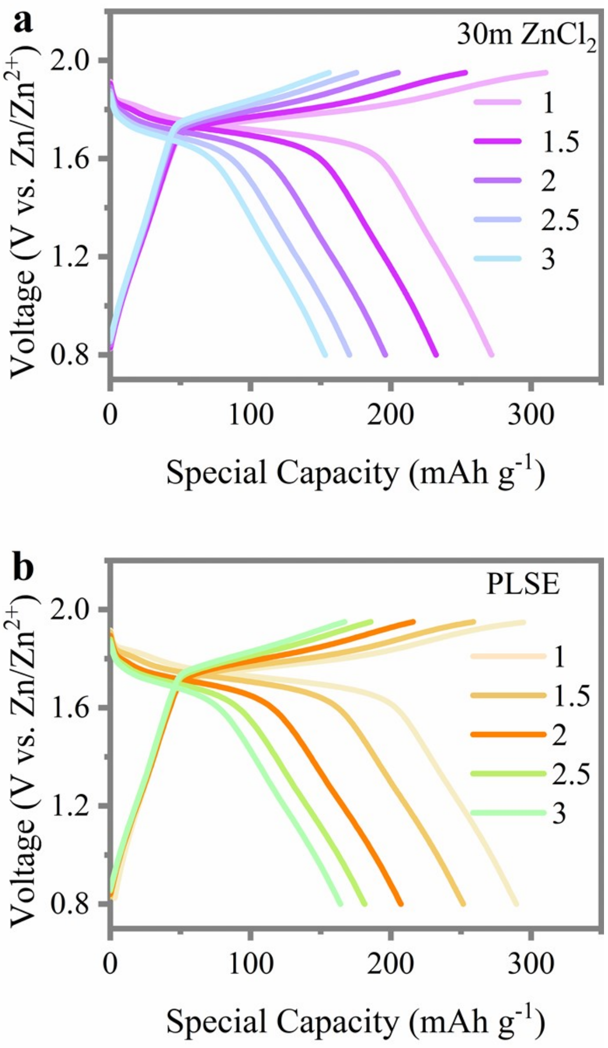

Fig. S43 GCD curves of Zn||Br_2 batteries assembled with (a) 30 m $ZnCl_2$ and (b) PLSE.

References

1. Yang X, *et al.* Aqueous zinc batteries with ultra-fast redox kinetics and high iodine utilization enabled by iron single atom catalysts. *Nanomicro Lett.* **15**, 126 (2023).
2. Sun F, *et al.* Theoretical advances in understanding and designing the active sites for hydrogen evolution reaction. *ACS Catal.* **12**, 8404-8433 (2022).
3. Zhang C*, et al.* A $ZnCl_2$ water-in-salt electrolyte for a reversible Zn metal anode. *Chem. Commun.* **54**, 14097-14099 (2018).
4. Santosh Kumar Samantaray*, et al.* Effect of phosphate ion on the textural and catalytic activity of titania–silica mixed oxide. *Appl. Catal., A* **220**, 9-20 (2001).
5. Hammett LP, *et al.* A series of simple basic indicators II Some applications to solutions in formic acid. *J. Am. Chem. Soc.* **54**, 4239-4247 (1932).
6. Hafner J. Ab-initio simulations of materials using VASP: Density-functional theory and beyond. *J. Comput. Chem.* **29**, 2044-2078 (2008).
7. Ghazy AR, *et al.* Investigating the differences in structure, morphology, optical properties, laser photoluminescence and dielectric properties for chitosan-doped commercial and Polycladia myrica mediated ZnO nanoparticles films combined with TD-DFT simulations. *Algal Res.* **71**, 103076 (2023).
8. Hu H*, et al.* Effect of Ring-Fusion on miscibility and domain purity: key factors determining the performance of PDI-based nonfullerene organic solar cells. *Adv. Energy Mater.* **8**, 1800234 (2018).
9. Kim JY, *et al.* Phase behavior of pi-conjugated polymer and non-fullerene acceptor (PTB7-Th:ITIC) solutions and blends. *Sci. Rep.* **12**, 20849 (2022).
10. Liu F, *et al.* Progress in the production and modification of PVDF membranes. *J. Membr. Sci.* **375**, 1-27 (2011).
11. Wang B, *et al.* Construction of a ternary system: a strategy for the rapid formation of porous poly(lactic acid) fibers. *RSC Adv.* **12**, 6476-6483 (2022).
12. Li DD, *et al.* Chemical compositions of improved model asphalt systems for molecular simulations. *Fuel* **115**, 347-356 (2014).
13. Cai S*, et al.* Water–Salt oligomers enable supersoluble electrolytes for high-performance aqueous batteries. *Adv. Mater.* **33**, 2007470 (2021).
14. Jiao S, *et al.* Descriptors for the evaluation of electrocatalytic reactions: d-band theory and beyond. *Adv. Funct. Mater.* **32**, 2107651 (2021).

15. J. K. Nørskov TB, *et al.* Trends in the exchange current for hydrogen evolution. *J. Electrochem. Soc.* **152**, J23-J26 (2005).

16. Raj V, *et al.* Direct correlation between void formation and lithium dendrite growth in solid-state electrolytes with interlayers. *Nat. Mater.* **21**, 1050-1056 (2022).

17. Al-Nafai I, *et al.* Aqueous stability relations in the hydrometallurgical processing of cerium bastnasite. *Miner. Process. Extr. Metall.* **131**, 34-43 (2020).

18. Jiang C*, et al.* A one-step aqueous route to prepare polyacrylonitrile-based hydrogels with excellent ionic conductivity and extreme low temperature tolerance. *J. Mater. Chem. A* **8**, 22090-22099 (2020).

19. Kopeć M, *et al.* Aqueous RAFT polymerization of acrylonitrile. *Macromol.* **49**, 5877-5883 (2016).

20. Ji X. A perspective of $ZnCl_2$ electrolytes: The physical and electrochemical properties. *eScience* **1**, 99-107 (2021).

21. Tian Z*, et al.* Electrolyte solvation structure design for sodium ion batteries. *Adv. Sci.* **9**, 2201207 (2022).

22. Jupp AR, *et al.* The global electrophilicity index as a metric for Lewis acidity. *Dalton Trans.* **47**, 7029-7035 (2018).

23. Xiao P*, et al.* An anticorrosive zinc metal anode with ultra-long cycle life over one year. *Energy Environ. Sci.* **15**, 1638-1646 (2022).

24. Yao Y-X, *et al.* Nucleation and growth mode of solid electrolyte interphase in Li-ion batteries. *J. Am. Chem. Soc.* **145**, 8001-8006 (2023).

25. Yang W, *et al.* Regulating water activity for rechargeable zinc-ion batteries: progress and perspective. *ACS Energy Lett.* **7**, 2515-2530 (2022).

26. Dong DJ, *et al.* Hydrotropic solubilization of zinc acetates for sustainable aqueous battery electrolytes. *Nat.* Sustainability **6**, 1474-1484 (2023).

27. Wang R, *et al.* Synergetic modulation on ionic association and solvation structure by electron- withdrawing effect for aqueous zinc-ion batteries. *Proc. Natl. Acad. Sci. U.S.A.* **120**, e2221980120 (2023).

28. Heng Jiang, et al. Chloride electrolyte enabled practical zinc metal battery with a near-unity Coulombic efficiency. Nat. Sustainability **6**, 806–815 (2023).

29. Gomez Vazquez D*, et al.* Creating water-in-salt-like environment using

coordinating anions in non-concentrated aqueous electrolytes for efficient Zn batteries. *Energy Environ. Sci.* **16**, 1982-1991 (2023).

30. Chen Z*, et al.* Polymeric single-ion conductors with enhanced side-chain motion for high-performance solid zinc-ion batteries. *Adv. Mater.* **34**, 2207682 (2022).

31. Lin C*, et al.* High-voltage asymmetric metal–air batteries based on polymeric single-Zn^{2+}-ion conductor. *Matter* **4**, 1287-1304 (2021).

32. Lu H*, et al.* Gradient electrolyte strategy achieving long-life zinc anodes. *Adv. Mater.* **35**, 2300620 (2023).

33. Wei Y*, et al.* Enabling all-solid-state li metal batteries operated at 30 °C by molecular regulation of polymer electrolyte. *Adv. Energy Mater.* **13**, 2203547 (2023).

34. Yang CY*, et al.* All-temperature zinc batteries with high-entropy aqueous electrolyte. *Nat. Sustainability* **6**, 325-335 (2023).

35. Chen L*, et al.* A 63 m superconcentrated aqueous electrolyte for high-energy Li-ion batteries. *ACS Energy Lett.* **5**, 968-974 (2020).

36. Li Y*, et al.* A superconcentrated water-in-salt hydrogel electrolyte for high-voltage aqueous potassium-ion batteries. *ChemElectroChem* **8**, 1451-1454 (2021).

37. Dai Y*, et al.* Reversible Zn metal anodes enabled by trace amounts of underpotential deposition initiators. *Angew. Chem. Int. Ed.* **62**, e202301192 (2023).

38. Han D*, et al.* A corrosion-resistant and dendrite-free zinc metal anode in aqueous systems. *Small* **16**, 2001736 (2020).

39. Wang W*, et al.* A dendrite-free Ga-In-Sn-Zn solid-liquid composite anode for rechargeable zinc batteries. *Energy Storage Mater.* **58**, 195-203 (2023).

40. Zhong Y*, et al.* An in-depth study of heterometallic interface chemistry: Bi-component layer enables highly reversible and stable Zn metal anodes. *Energy Storage Mater.* **55**, 575-586 (2023).

41. Meng Y*, et al.* Balancing interfacial reactions through regulating p-band centers by an indium tin oxide protective layer for stable Zn metal anodes. *Angew. Chem. Int. Ed.* **62**, e202308454 (2023).

42. Liu W*, et al.* Metallic Particles-Induced surface reconstruction enabling highly durable zinc metal anode. *Adv. Funct. Mater.* **33**, 2302661 (2023).

43. Fayette M, *et al.* High-performance InZn alloy anodes toward practical aqueous zinc batteries. *ACS Energy Lett.* **7**, 1888-1895 (2022).

44. Liu C*, et al.* Liquid alloy interlayer for aqueous zinc-ion battery. *ACS Energy Lett.* **6**, 675-683 (2021).

45. Zhou Y*, et al.* A dendrite-free Zn anode co-modified with In and ZnF_2 for long-life Zn-Ion Capacitors. *ACS Appl. Mater. Interfaces* **14**, 46665-46672 (2022).

46. Ouyang K*, et al.* A new insight into ultrastable Zn metal batteries enabled by in situ built multifunctional metallic interphase. *Adv. Funct. Mater.* **32**, 2109749 (2021).

47. Li X*, et al.* Activating the I^0/I^+ redox couple in an aqueous I_2–Zn battery to achieve a high voltage plateau. *Energy Environ. Sci.* **14**, 407-413 (2021).